MATERIALS DISCOVERY USING IN SITU REDUCTION AND X-RAY DIFFRACTION

BY

REBECCA D. MCAULIFFE

DISSERTATION

Submitted in partial fulfillment of the requirements
for the degree of Doctor of Philosophy in Materials Science and Engineering
in the Graduate College of the
University of Illinois at Urbana-Champaign, 2018

Urbana, Illinois

Doctoral Committee:

- Assistant Professor Daniel P. Shoemaker, Chair
- Professor Jian-Min Zuo
- Assistant Professor Nicola H. Perry
- Professor S. Lance Cooper

ABSTRACT

Materials discovery is important for pushing new and existing technologies forward. In this thesis, a systematic approach to materials discovery is presented that highlights the combined use of in situ reduction reactions and X-ray diffraction to quickly explore compositional space. Reduction reactions provide a synthesis route that has been shown to gently traverse a compositional space. Traditional synthesis at high temperatures tends to only favor the formation of thermodynamically stable compounds, however, with a more controlled synthesis route, kinetically stable and metastable compounds may be easier to discover.

By coupling reduction reactions with in situ X-ray diffraction, intermediate and metastable phases can be observed. Once a phase is observed using in situ X-ray diffraction, attempts can be made to stabilize the phase ex situ in order to solve the structure and understand the material's properties. In this thesis, an in situ cell is described that can be used to perform these in situ reduction reactions using a laboratory X-ray diffractometer. Since the technique can now be performed on a laboratory scale, rapid phase exploration can be performed.

This combined approach will be discussed with regard to two different materials systems, K-Sn-O and Fe-S. In the K-Sn-O system, in situ and ex situ studies are performed in order to search for new *p*-type transparent conducting oxides. In the Fe-S system, in situ reduction is used to solve a highly debated question of whether or not pyrite FeS_2 is a non-stoichiometric compound and to quantify the possible extent of non-stoichiometry.

For my family

ACKNOWLEDGMENTS

I would like to first thank Daniel Shoemaker for all of his advice and guidance. This work would not be possible without him. When I joined Daniel's group, I was worried because I had very little chemistry experience, but from the beginning Daniel has stood by my side helping me to become a better researcher. He was supportive when I was overwhelmed and celebrated my achievements both personal and professional. Lastly, he brought me into the solid state chemistry community where I am excited to continue my work.

Thank you to Ankita and Zhelong for being great labmates. It was a pleasure setting up the lab with them and having long discussions in the office about work and the world. I really appreciate the friendship that we have and research would not have been as fun without them both. Thank you to Chris, Ben, and Shuai for their assistance on understanding the K-Sn-O system. Each of them was very patient with this confusing system and provided many samples throughout the process. Thank you to the rest of the Shoemaker group, I really enjoyed working with each one of them.

Thank you to Sandy and Kimberly for answering my endless questions about logistics and requirements. I enjoyed having long conversations with the both of them whenever I went to the Materials Science Building. They always made me smile and feel welcome. Also, thank you to Doug, Susie, Dawn, and the rest of the MRL staff. They always took time to answer my questions and help my research run as smoothly as possible.

Thank you to Andrew Kunz for his support at Marquette University. He was always there to listen to my ever-changing goals. His excitement about magnetism and solid state physics has stuck with me and motivated me to attend UIUC. Even after graduating from Marquette

University, he still took time to discuss research and graduate school experiences with me.

Thank you to all of my family for their support and words of encouragement throughout the years. Everyone has been excited about my work, even if they do not always understand what I am working on. Also, thank you to my parents. They both taught me a lot throughout the years and are always excited to hear about my latest adventures.

A huge thank you to Jon for his patience and support. From the beginning of our relationship, he supported me in achieving my goals even when it meant moving further apart. I am excited to see what the future holds with you at my side, rather than four hours away.

Lastly, I would like to thank the friends that I made at UIUC, specifically Scotty, Charles, Blanka, Aidan, and Kaitlin. The past years would not have been the same without each of them. They all supported me and listened to my constant ramblings about research and life.

To everyone else, thank you for helping to make these past years a success.

TABLE OF CONTENTS

LIST OF TABLES

LIST OF FIGURES

CHAPTER 1

MATERIALS DISCOVERY

New materials with enhanced properties are needed to advance technologies. With new goals to create better batteries, thermoelectrics, and superconductors, materials science has made a large effort to rapidly expand the set of known compounds. This search for unknown materials is often performed by trial-and-error, but as the compositional space moves into ternary, quaternary, and higher order systems, a more systematic approach is needed. This study outlines one approach to discovering new materials using reduction reactions and in situ X-ray diffraction.

1.1 System Selection

In order to have a directed search for new materials, care must be taken in selecting the material systems to explore. In this study, three main criteria were taken into consideration when choosing a system to study: the application of interest, the extent of previous studies performed, and the likely number of minima in the system's energy landscape.

It is beneficial to start a search for new materials with a desired property or application in mind. By choosing a property or application, a large portion of compositional space can often be ignored. For example, this study focuses on the discovery of new materials for *p*-type transparent conducting oxide (TCO) applications. By only choosing oxide compounds, the total number of potential ternary systems is reduced from 10^6 to 10^4 systems.

While several *n*-type TCO materials have been discovered and are used commercially, *p*-type TCOs have lagged behind. This is because, in metal oxides, the valence band maximum consists of localized O 2*p* orbitals that create large effective masses for carriers and make doping difficult.[1] In order to increase the mobility of carriers, their effective mass must be decreased. One way to change the valence band bonding character and decrease the effective mass of carriers is by including elements with filled *d* or *s* orbitals. Materials with these bonding states near the O 2*p* level have been shown to create hybridized orbitals that improve *p*-type TCO behavior.[2, 3] This was first shown in $CuAlO_2$, leading to the investigation of many Cu-based *p*-type TCOs.[4] By understanding the necessary design parameters for a specific property or application, the vast potential compositional space can be restricted. In the case of *p*-type TCOs, the search can be limited to oxides that contain a cation with filled *d* or *s* orbitals that will hybridize with the O 2*p* orbital. This hybridization has been shown in compounds containing Cu^{+}, Sn^{2+}, Pb^{2+} and Bi^{3+}.[5, 3, 6, 7, 8]

Understudied systems are preferred to those that have been more extensively searched. In systems that have been explored with a range of synthetic techniques, there is less likely to be an undiscovered phase. In understudied systems, however, relatively little space has been searched and a more extensive study could yield a number of unknown compounds. For example, binary Sn-O phases have been extensively studied and characterized for TCO applications, but many ternary *A*-Sn-O systems have not been studied as heavily. For *A*-Sn-O systems, where *A* is an alkali element, very few studies have been performed. In the K-Sn-O system, for example, only studies using KNO_3 and SnO_2 have been explored previously.[9] Having only been the focus of a few studies, there is an opportunity to discover new compounds via a variety of synthesis conditions.

Lastly, it is important to consider the density of a system's energy landscape. The energy landscape can be described as a surface associated with all possible atom configurations where all energy minima are associated with a possible phase. These phases could be thermodynamically or kinetically stable and are all realizable.[10] In order to identify these possible phases, a thorough search of the energy landscape must be performed. It has been shown that crowded phase diagrams are more likely to yield new phases due to the complex energy landscape.[11]

Alkali-Sn-O systems are relatively underexplored and show promise for TCO applications. This study will focus on the exploration of the K-Sn-O system to discover new phases for TCO applications.

1.2 Reduction Reactions

Reduction reactions can be used to explore dense phase spaces since the reduction potential can be adjusted by changing the type of reducing agent and reaction temperatures. Reduction can provide a means of investigating phase space gently in order to find new phases that may exist in dense energy landscapes.

Reduction reactions can be performed on known, stable structures to carefully investigate the surrounding phase space. Topotactic transitions are known to occur upon reduction of a parent compound in which the resulting phase has a 3D similarity to the initial phase structure. This type of reduction occurs as the anions are gently removed from the lattice, leaving the cation lattice intact. Topotactic reduction reactions are an important synthetic route to discover new phases. New anion-deficient structures have been discovered that possess a wide range of magnetic and electronic behaviors that are different than their parent compounds.[12, 13]

In this study, reduction reactions are a crucial synthesis route to form new materials in the K-Sn-O system. This is because potential precursors such as KO_2, K_2O, and K_2CO_3 are all hygroscopic and difficult to weigh properly. Reduction reactions provide a means to look for new compounds by starting with stable compounds with known synthesis conditions and gently probe for phases with a lower oxidation state. This reduction of Sn^{4+} is especially important since Sn^{2+} have filled *s* states, which are an important design criteria for new *p*-type TCOs, as discussed previously.

Reduction reactions can also be utilized as a means to study the stoichiometry ranges of compounds and the formation of defects, specifically vacancies, within the lattice. Changes in stoichiometry are important to understand and quantify as many material properties are related to the overall stoichiometry of the material. This is especially true in systems such as semiconductors and magnetic materials, where relatively small compositional changes can have a large impact on properties.[14, 15, 16]

For example, pioneering measurements on the topotactic reduction of $Y_2Ti_2O_{7-x}$ by Hayward were used to show the relationship between non-stoichiometry and magnetic properties when samples were slightly reduced.[17] Also, studies performed on anatase $TiO_{2-\delta}$ show that the sample's conductivity is heavily dependent on the oxygen composition.[18]

In this study, reduction reactions provide a route to investigate the extent of non-stoichiometry of iron sulfides. The long debated question of whether or not FeS_2 has a region of non-stoichiometry can be directly studied using in situ reduction reactions which will be discussed in Chapter 5.

1.3 Characterizing New Materials

Structure solutions of unknown compounds using powder diffraction is challenging. To assist in determining the structure of a new compound, complementary techniques must be used. Material characteristics such as stoichiometry and the presence of functional groups help assist in the structure solution as they provide chemical constraints. Many characterization techniques can be utilized alongside diffraction to understand a new material. A few of the techniques that were essential to this study are explained in this section.

1.3.1 X-ray Spectroscopy

Scanning electron microscopy (SEM) with energy dispersive X-ray spectroscopy (EDS) detects the secondary X-rays emitted due to X-ray fluorescence. In the case of SEM-EDS, incident electrons eject the electrons from the material. The ejected electrons are then replaced by electrons from higher energy levels. The transition results in the emission of a photon whose energy is equal to the energy difference between the two states of the electron. These discrete energy levels are different for each atom and, therefore, the photon energies can be used to determine the elemental composition of the material. [19]

SEM-EDS is useful for samples in which impurity phases are present because measurements can be performed on individual particles to determine their elemental composition. The comparison of the composition of an unknown compound with that of a known material with a fixed composition gives higher confidence in the measured composition. However, non-conductive materials must be coated with a conductive layer to prevent the sample from charging in the electron beam. The elements in the coating will be present in the EDS spectra and the samples cannot be used for further study.

1.3.2 C,H,N Analysis

Commonly used for small molecule analysis, C,H,N analysis can assist in detecting lighter elements that could form functional groups in synthesized materials. In C,H,N analysis, the sample is placed in a capsule inside a heating furnace. Once placed in the heating furnace, the sample is combusted in pure oxygen at temperatures reaching over 1800°C.

After the total combustion of all inorganic and organic compounds, the gaseous products pass through a variety of reagents in order to produce CO_2, H_2O, and N_2 and to remove other products such as S. These gases pass through a series of three thermal conductivity detectors with a pair of thermal conductivity cells. The first cell acts as a water trap where the signal is proportional to the amount of water present. The second cell acts as a CO_2 trap to measure the presence of carbon. The last cell is measured against a helium reference to measure the amount of N_2 present.[20]

C,H,N analysis is necessary to understand the possible functional groups on discovered compounds. This is of particular interest if the system is prone to form hydroxides and hydrated phases. C,H,N analysis is a fast way to determine whether or not the material formed is an oxide. This technique is also useful to detect the possible presence of unreacted carbonate precursors that are difficult to observe using laboratory X-ray diffraction in small quantities.

1.3.3 FTIR Spectroscopy

Fourier transform infared (FTIR) spectroscopy is performed by passing infared (IR) radiation through a sample creating a spectra that is specific to the sample. Infared light is absorbed when an electric dipole moment changes during the movement of a group of atoms. This movement corresponds to a bending or stretching of the bonds. Since certain functional groups have known vibrational modes, they can be identified within the FTIR spectra. For example, O-H stretching creates a broadband that is observed between 3200-3700 cm^{-1}.[21] In this study, the FTIR spectra is used to determine whether compounds are hydroxides, hydrates, or oxides.

1.4 Crystal Structure Analysis

The structure of the material is very important to determine as this can help to explain and understand the material's overall properties. There are several main ways of determining the structure of a material from powder diffraction data. In structure solution, the main problem is in finding the structure that resides with a minimum global energy that follows chemical bonding criteria. Many structures may be possible with a minimum local energy, but do not accurately explain the true crystal structure of the sample.

1.4.1 Simulated Annealing

Simulated annealing is a computational technique that can be used to solve crystal structures of compounds by optimizing an atomistic model using high quality diffraction data and chemical constraints. This technique is based on the process of annealing solids in which the material is heated and allow to cool slowly until it achieves the most stable lattice configuration.[22]

Simulated annealing allows ”hill-climbing” moves that allows the system to escape local minima in order to find the global minimum.[23] When choosing a structure, structures that improve the fit are always accepted, however a fraction of the solutions that do not improve the fit are accepted in order to escape local minima. The acceptance rate of new solutions is selected based on the Metropolis acceptance criterion. The acceptance probability is shown in equation 1.1, where $f(w)$ is the energy of the current solution and $f(w')$ is the energy of the next solution being tested.[23]

$$P(\text{Accept } w' \text{as next solution}) = \begin{cases} exp[-(f(w') - f(w))/t_k] & \text{if } f(w') - f(w) > 0 \\ 1 & \text{if } f(w') - f(w) \leq 0 \end{cases} \tag{1.1}$$

$$t_k > 0 \text{ for all } k \text{ and } \lim_{k \to +\infty} t_k = 0 \tag{1.2}$$

Simulated annealing mimics physical annealing by having a higher probability of changing configuration in the initial steps and while ”cooling” the probability of switching is decreased as the system should settle into the lowest energy state. This ”temperature” term is shown in equation 1.2.

One major downside to simulated annealing is that it is a time-intensive technique. When defining a temperature profile, a significant amount of time must be spent at high temperatures to allow for the structure to move out of local minima. However, at high temperatures a significant amount of time can be spent in improbable structures because of the higher switching probability.

1.4.2 Rietveld Refinement

Once the structure of a material is known, the Rietveld refinement method can be used to refine the structural parameters for a given sample and diffraction pattern. The Rietveld refinement method is a least-squares refinement that compares a calculated diffraction model to the observed diffraction pattern.[24] Physical properties of the material are used to construct the calculated pattern and are refined in order to minimize the Equation 1.3, where y is the intensity of the observed or calculated pattern at a given point and w is a statistical weighting factor. A common weight factor is shown in Equation 1.4, where a larger weight is given to peaks with a lower intensity.

$$M = \sum_{i=1}^{N} w_i [y(obs)_i - y(calc)_i]^2 \tag{1.3}$$

$$w_i = \frac{1}{y(obs)_i} \tag{1.4}$$

Many different equations are used to calculate the goodness of fit or R-factor for Rietveld refinement analyses.[25, 26] In this study, the weighted profile R factor, shown in Equation 1.5, is reported to determine the accuracy of the calculated fit.

$$R_{wp} = [\frac{\sum_i w_i [y(obs)_i - y(calc)_i]^2}{\sum_i w_i y(obs)_i^2}]^{\frac{1}{2}} \tag{1.5}$$

Rietveld refinements provide important quantitative structural information such as unit cell parameters, atomic positions, and site occupancies that can be used to understand the material's structure and resulting properties.

CHAPTER 2

STRUCTURE SOLUTION AND PROPERTIES OF $K_2Sn_3O_7$

2.1 Introduction

Tin-containing oxides form the basis of many electronic device technologies, including the quintessential n-type transparent conducting oxides (TCOs) In_2O_3 and SnO_2 [27]. SnO_2 has been investigated as a TCO [28] and Li-ion battery anode,[29, 30] along with other compounds derived from octahedral SnO_6 units, including spinel-type Zn_2SnO_4 [31, 32] and mixed hollandites such as $K_2(M Sn_6)O_{16}$ and $K_2(M Sn_7)O_{16}$ where M = Mg, Fe, Mn, or Ga.[33].

Binary oxides with filled d states and wide band gaps such as SnO_2 and Ga_2O_3 are potential candidates for p-type TCOs, but their performance is limited by low hole mobility, which resides in the O p states at the Fermi energy.

In contrast to SnO_2, oxides of Sn^{2+} with a $5p^2$ electron configuration such as SnO have Sn s and p_z mixed with O p-orbital character near the valence band maximum, with more dispersed bands that may indicate higher mobility in the absence of unfavorable defects.[34, 7] Subsequent doping leading to an effective p-type TCO remains elusive, but has been proposed for SnO [8] and systems with additional ions, such as $K_2Sn_2O_3$ [35].

In order to investigate new oxides that can host Sn in either valence state, understudied

---

Reproduced in part with permission from R. D. McAuliffe, C. A. Miller, X. Zhang, B. S. Hulbert, A. Huq, C. dela Cruz, A. Schleife, and D. P. Shoemaker, Structural, electronic and optical properties of $K_2Sn_3O_7$ with an offset hollandite structure. *Inorg. Chem.* **56** (5) 2914-2918 (2017), ©2017 American Chemical Society ternary phase spaces are of interest. Detailed investigations of phase equilibria in the systems A–Sn–O, where A is an alkali, are rare. This may be because many of the precursors (alkali oxides and carbonates) are hygroscopic. K_2CO_3 noticeably absorbs water when being weighed in air, as does K_2O. The products of these reactions, however, can be quite stable. In 2002, a report by Iwasaki *et al.* presented the new compound $Na_4Sn_3O_8$ from the reaction of Na_2CO_3 and SnO_2 at 1300° C.[36]

The K–Sn–O system contains five phases with known crystal structures. There are two Sn^{4+} compounds K_2SnO_3 and K_4SnO_4,[37, 38] as well as the Sn^{2+} compounds K_2SnO_2, $K_2Sn_2O_3$, and K_4SnO_3.[39, 40, 41, 42] A compositional map with known K-Sn-O phases is shown in Figure 2.1 Tournoux performed the only systematic phase equilibria study on this system [9]. His elemental analysis of a K_2SnO_3 decomposition product revealed an estimated stoichiometry $K_2Sn_3O_7$, but the structure was never solved. Here, a single-step synthesis for this compound, its crystal structure, and optical characterization are presented. $K_2Sn_3O_7$ has a unique structure type among oxides, reminiscent of an offset hollandite with bowtie-shaped channels, which is shared only with the recently-discovered compound $Cs_2U_3Se_7$.[43]

2.2 Methods

Powdered K_2CO_3 and SnO_2 were ground by hand in an agate mortar and pestle with molar ratios of 4:1, 3:1, and 2:1 K:Sn. Each mixture was pressed into 12 mm-diameter pellets and fired in air, inside beds of sacrificial powder in uncovered alumina crucibles. The samples were fired at 900° C for nine hours with heating and cooling rates of 10° C/min.

Powder diffraction was performed using a Bruker D8 diffractometer with Mo-K_α radiation and a capillary mount, with samples mixed with SiO_2 to reduce absorption. Neutron powder diffraction was performed on the POWGEN instrument at the Spallation Neutron Source on air-exposed samples.

The structure was initially solved using the FOX software,[44] fitting to X-ray diffrac-

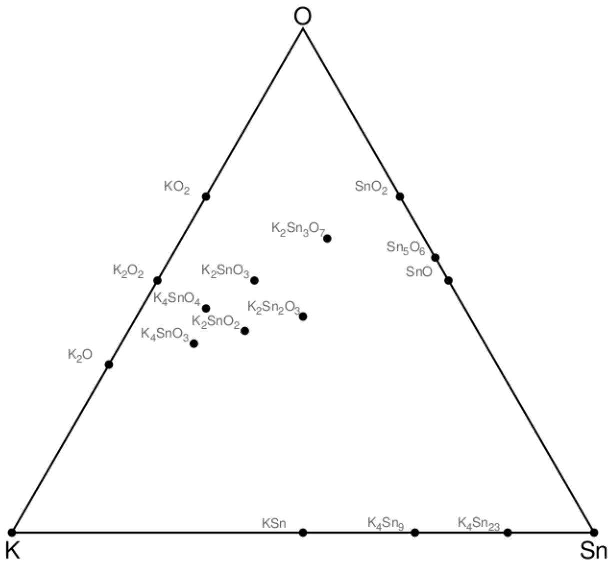

Figure 2.1: Compositional map of the K-Sn-O system

tion (XRD) data. Rietveld refinements to X-ray and neutron data were performed using GSAS.[45] Structures were plotted using VESTA [46].

Scanning electron microscopy (SEM) was performed using a JEOL 6060LV with energy dispersive X-ray spectroscopy (EDS). Optical spectroscopy was performed in diffuse reflectance geometry with a Cary 5000 UV-VIS-NIR spectrometer.

2.3 Results and Discussion

$K_2Sn_3O_7$ forms as a quantitative product of the decomposition of K_2CO_3 and SnO_2. It is surprising that such a common reagent combination, in air, forms a compound that is unsolved and unique among oxides. Excess carbonate is left unreacted or vaporized, depending on the duration of the reaction. Using a K:Sn ratio less than 2:3 in the reagents leads to the presence of excess SnO_2. In that case, $K_2Sn_3O_7$ seems to be the only ternary product of these reactants in air. Reactions conducted below 830° C are incompletely reacted, and the compound is stable in air up to the maximum temperature attempted, 1000° C.

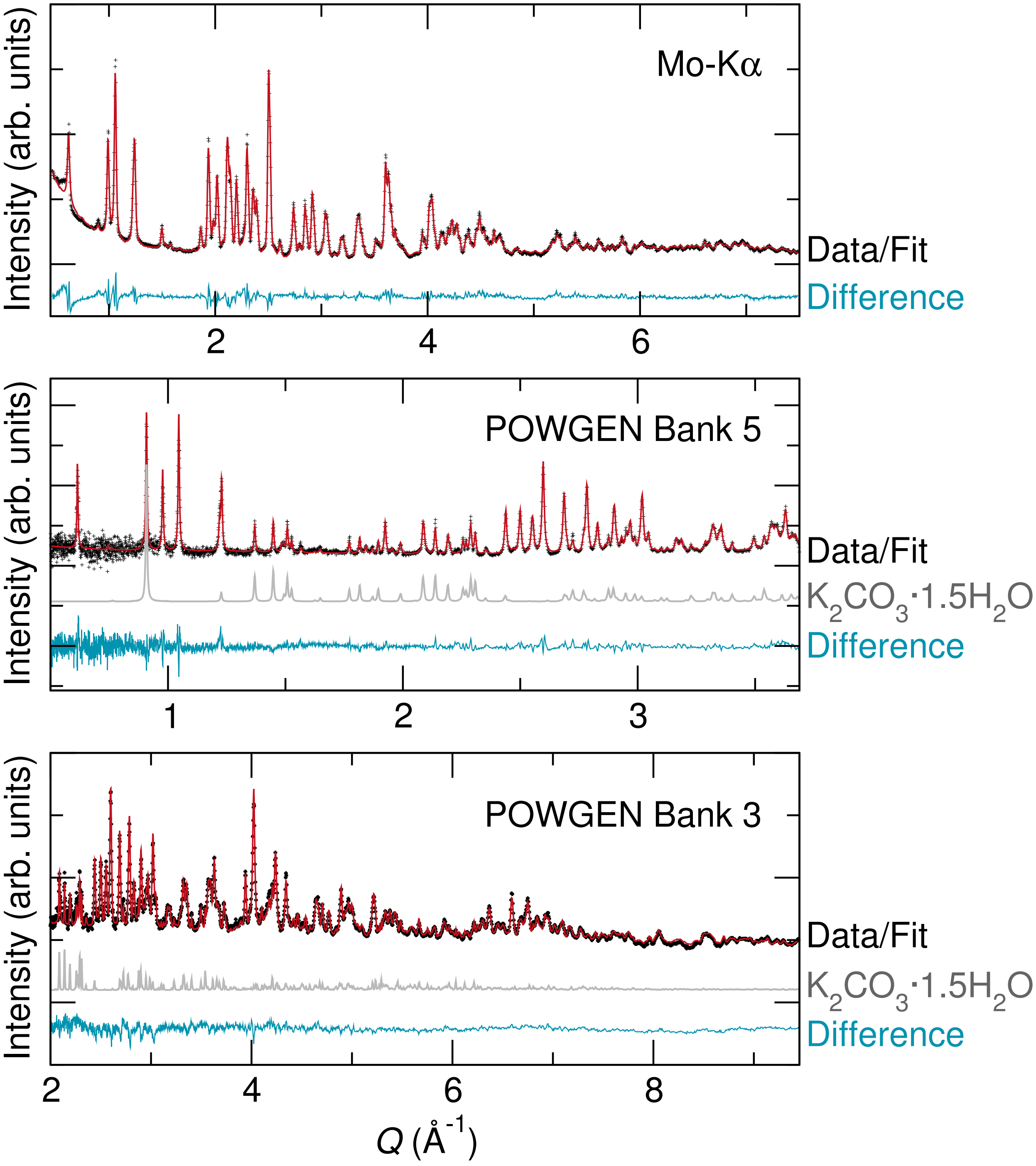

Figure 2.2: Rietveld refinements to laboratory X-ray data (top) and two banks of time-of-flight neutron powder diffraction for $K_2Sn_3O_7$. The large X-ray scattering factor for Sn necessitates neutron diffraction measurements to reliably refine the oxygen displacement parameters. The peak profile is shown in gray for a second phase $K_2CO_3 \cdot 1.5H_2O$ that was not present in the XRD data. Reproduced with permission from reference [47], ©2017 American Chemical Society

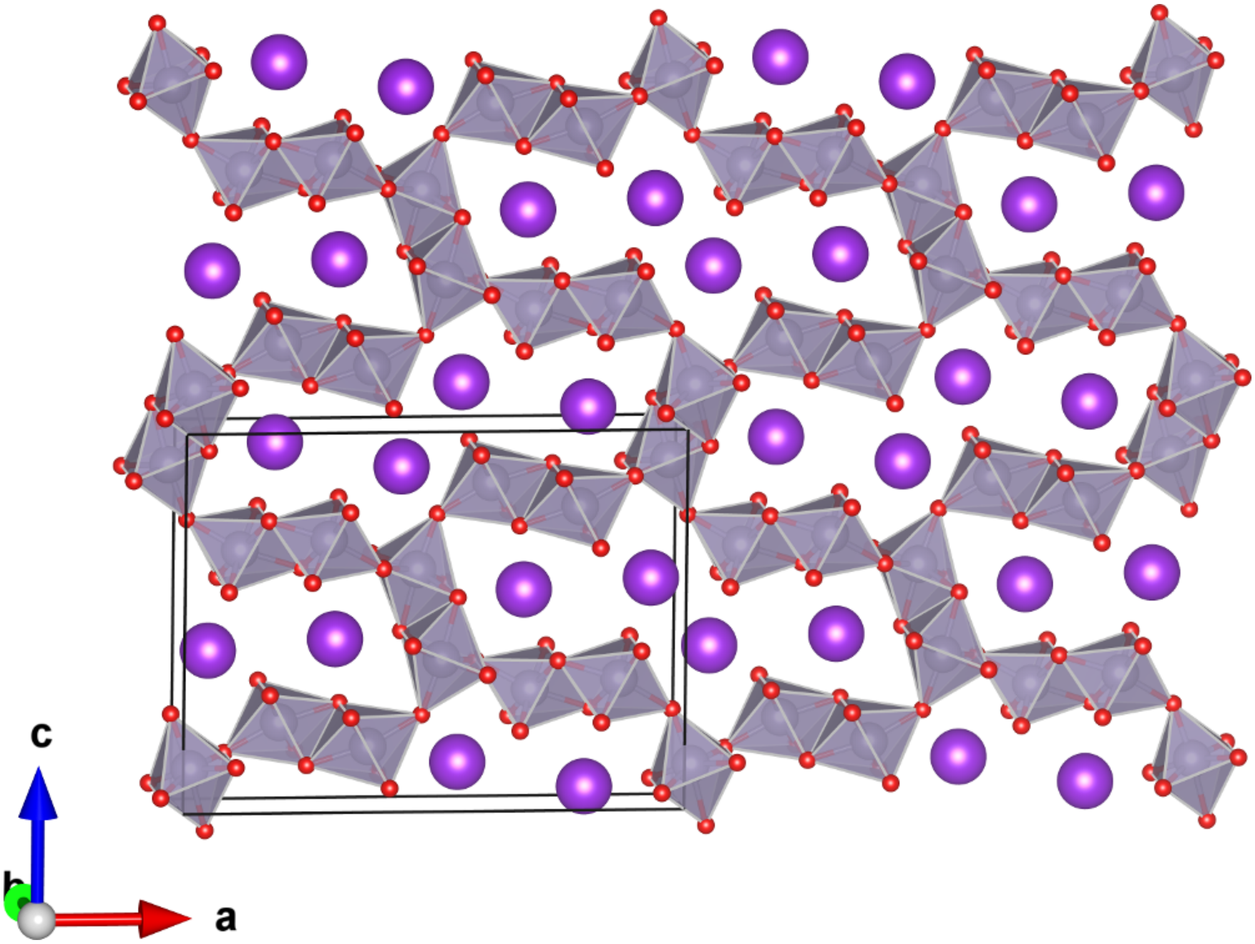

Figure 2.3: 2 × 1 × 2 view of $K_2Sn_3O_7$, with the unit cell shown, as refined from neutron powder diffraction with K in purple, O in red, and Sn shown in gray octahedra. The short *b* axis implies that the structure forms one-dimensional channels of K^+ ions into the page. Reproduced with permission from reference [47], ©2017 American Chemical Society

Rietveld refinements are shown in Fig. 2.2 for XRD data and two banks of time-of-flight neutron diffraction data from POWGEN. The XRD data appears phase-pure, while a small amount (9 wt%) of $K_2CO_3{\cdot}1.5H_2O$ is evident in the neutron diffraction data. The invisibility of the carbonate to XRD may arise from the much stronger scattering power of Sn in XRD data. For the same reason, neutron diffraction was required to refine the positions and atomic displacement parameters of the 7 oxygen positions in the cell. No carbonate impurities were seen in EDS or backscattered SEM imaging of the samples used for UV-vis analysis.

The structure of $K_2Sn_3O_7$ is shown in Fig. 2.3 and parameters are given in Table 2.1. The structure forms with a very short orthorhombic *b* axis of 3.12 Å, which corresponds

Table 2.1: $K_2Sn_3O_7$ structure as refined from POWGEN neutron diffraction data. Space group $Pnma$, a=16.8640(4) Å, b=3.12250(8) Å, c=12.8523(5) Å. U_{iso} units are 10^{-2} Å^2. Reproduced with permission from reference [47], ©2017 American Chemical Society

Atom	x	y	z	U_{iso}
Sn1	0.0120(3)	0.25	0.1086(4)	0.83(8)
Sn2	0.2916(3)	0.25	0.7084(4)	0.9(1)
Sn3	0.3730(3)	0.25	0.1649(4)	1.2(1)
K1	0.3073(7)	0.25	0.447(1)	6.3(4)
K2	0.4346(5)	0.25	0.8967(9)	4.5(4)
O1	0.0934(3)	0.25	0.5737(4)	1.6(1)
O2	0.1725(4)	0.25	0.7584(4)	1.2(1)
O3	0.1767(4)	0.25	0.3008(4)	1.8(1)
O4	0.2517(4)	0.25	0.1144(4)	1.1(1)
O5	0.4007(3)	0.25	0.6318(4)	1.1(1)
O6	0.4802(3)	0.25	0.2463(4)	2.1(1)
O7	0.5503(4)	0.25	0.5530(4)	0.7(1)

to a single O–O distance and portends the one-dimensional, channel-type structure that is typical of hollandites, among other compounds. To date, tin has been shown to form only substituted hollandites of the type $K_2MSn_7O_{16}$ (monoclinic $C2/c$) and $K_2MSn_7O_{16}$ (tetragonal $I4/m$), where M=Mg, Fe, Mn, and Ga [48, 33]. Both of these form channels bound by 2 × 2 arrangements of SnO_6 octahedra enclosing a single row of alkali ions. In $K_2Sn_3O_7$ the channels are significantly more open, creating a four-cation alkali channel with a zigzag shape that is apparent in the structure in Fig. 2.3.

SEM investigation of crushed $K_2Sn_3O_7$ pellets revealed porous agglomerates visible in Fig. 2.4, with some large agglomerates remaining such as the piece in Fig. 2.4(b). EDS analysis gave K:Sn ratios around 2:3, which were used with the unit cell obtained by FOX to solve for the number of Sn ions on the cell. Closer inspection of these agglomerates reveals them to consist of needle-shaped grains, which are around one micron in width and tens of microns in length. Electron backscatter imaging in Fig. 2.4(c) does not reveal any substantially higher- or lower-Z-density regions that would indicate impurities.

The band gap of $K_2Sn_3O_7$ is difficult to characterize using UV-Vis spectroscopy since it is wide enough to approach the edge of the detector. However, the downturn in reflectivity around 3 eV is apparent, with nearly full absorption occurring around 4 eV in Fig. 2.5. As

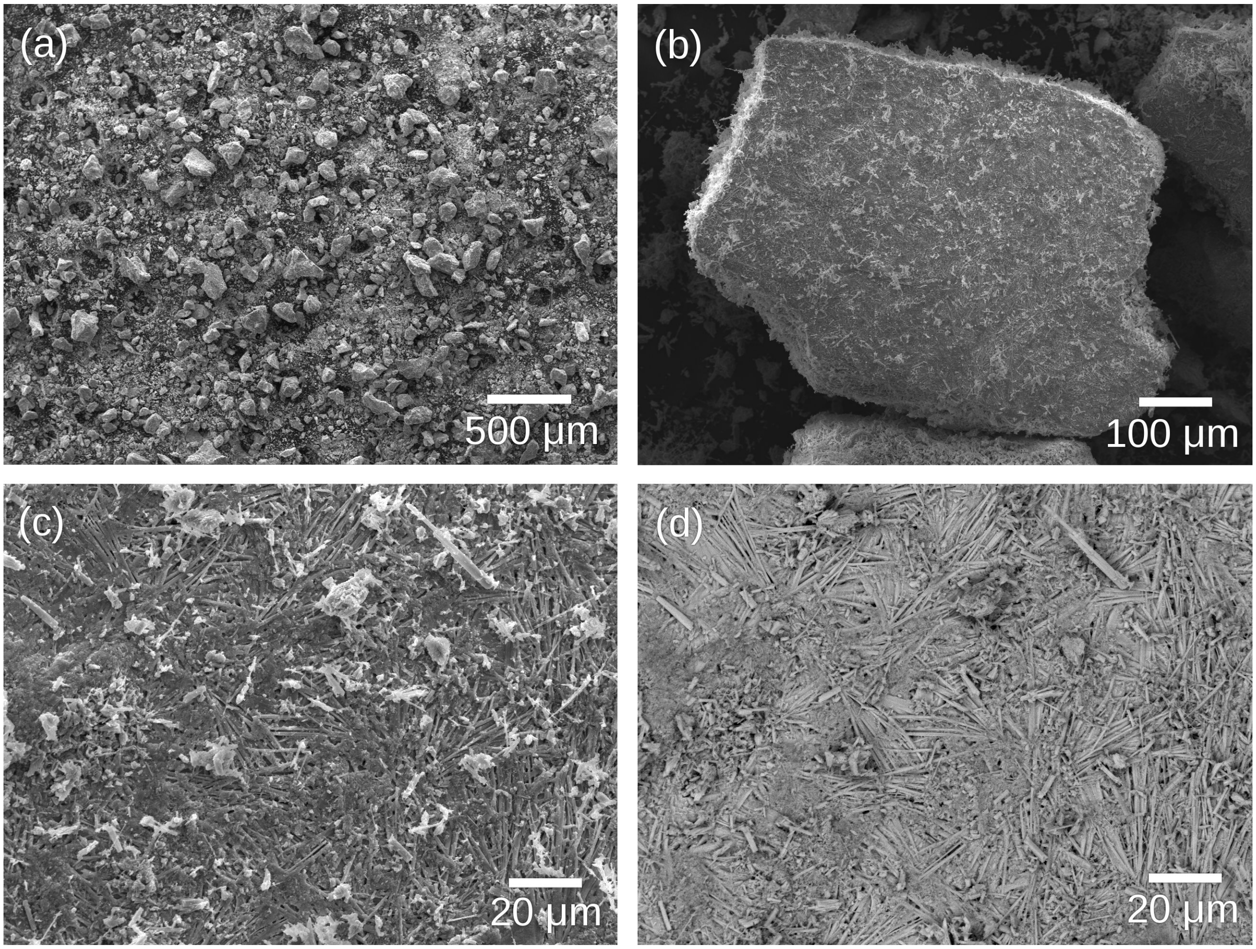

Figure 2.4: Scanning electron micrographs in secondary electron imaging (a-c) reveal a mixture of fine and agglomerated powder comprised of micron-scale fused rods. Backscattered electron imaging (d) of the area in (c) indicates that the non-rod-shaped particles on the agglomerate surface are the same composition. Reproduced with permission from reference [47], ©2017 American Chemical Society

a comparison, rutile-type SnO_2 (cassiterite) has a known band gap around 3.6 eV [49].

2.4 Conclusion

The structure of $K_2Sn_3O_7$ was solved from powder diffraction and refined its structure to X-ray and neutron scattering data. This material is isostructural with only one compound, $Cs_2U_3Se_7$, and is the first oxide with this structure type. It forms in air from common reagents, and has 1-dimensional channels that are reminiscent of a hollandite structure that

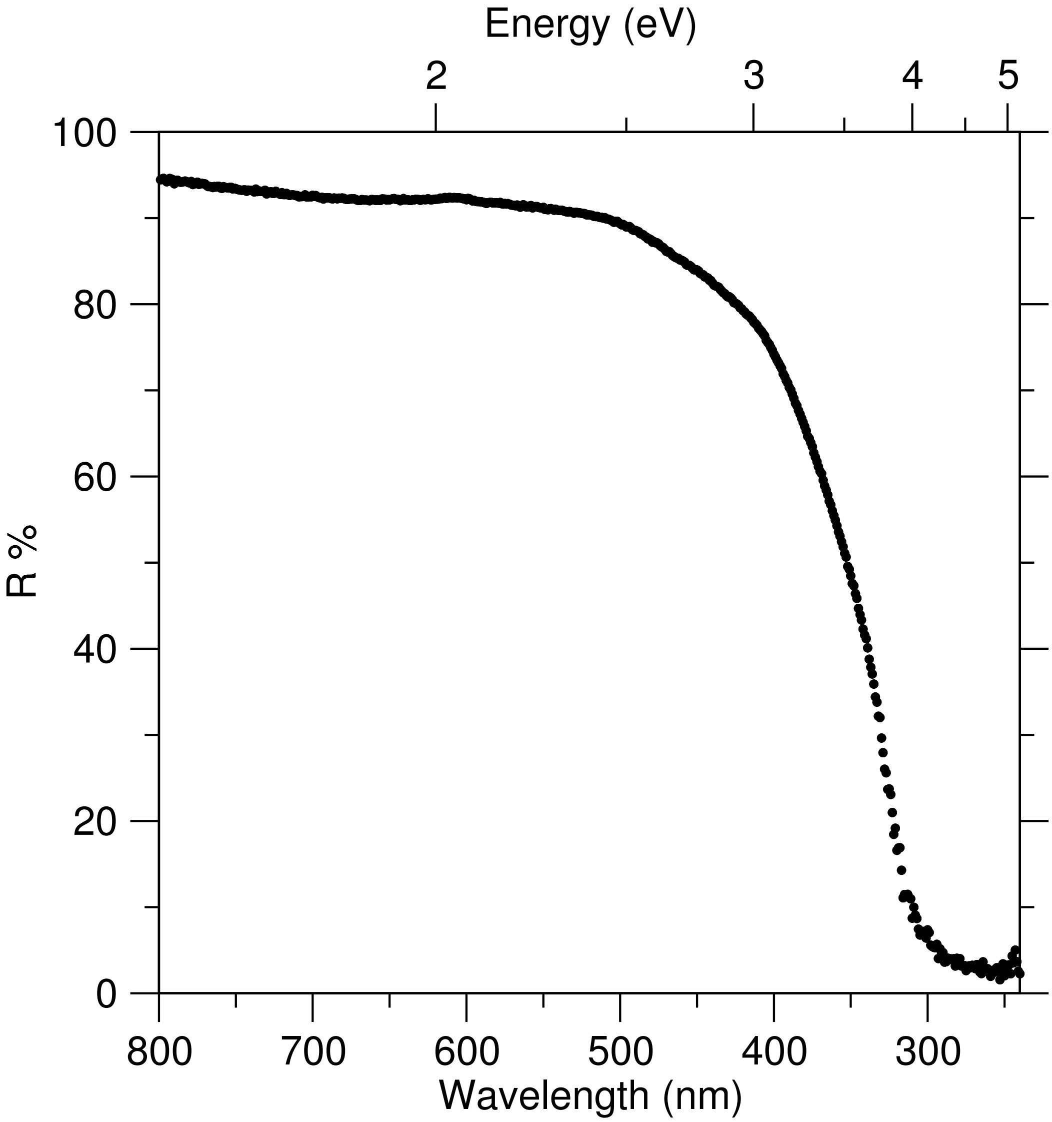

Figure 2.5: UV-Vis spectroscopy of powdered $K_2Sn_3O_7$ shows a large band gap, approximately 3 eV. Reproduced with permission from reference [47], ©2017 American Chemical Society

has been partially opened. The mobility of K^+ ions, their propensity to undergo cation exchange, and the redox behavior of $K_2Sn_3O_7$ remain to be investigated.

CHAPTER 3

STRUCTURE SOLUTION AND PROPERTIES OF $K_2Sn_4O_9$

3.1 Introduction

In order to optimize the synthesis of $K_2Sn_3O_7$ and eliminate the $K_2CO_3 \cdot 1.5H_2O$ observed in neutron diffraction, the potassium precursor was switched from K_2CO_3 to KO_2. In some reactions, a new phase was observed, but was difficult to replicate. This phase seemed to form when $K_2Sn_3O_7$ is stored in air for several months.

When testing the water stability of $K_2Sn_3O_7$, the phase was observed once again. By optimizing the amount of time the powder was in water and drying conditions, the phase was isolated. The phase matches a description of a $K_2Sn_4O_9$ phase observed by Tournoux, but no structure or compositional study was performed.[9] Here, a study of the isolated $K_2Sn_4O_9$ phase is presented.

3.2 Methods

$K_2Sn_3O_7$ was synthesized using KO_2 and SnO_2 in a molar ratio of 2:3 K:Sn. KO_2 and SnO_2 were ground by hand in an agate mortar and pestle in a N_2 filled glove bag. The mixture was fired in an uncovered alumina crucible at 900°C for 9 hours in a N_2 atmosphere. The mixture was heated in a box furnace with heating and cooling rates of 10°C/min.

$K_2Sn_4O_9$ was synthesized by placing $K_2Sn_3O_7$ in 50mL of DI water. The DI water was placed on a hot plate set to 200° C for 1 hour and was magnetically stirred at a 300 rpm throughout. The powder was separated from the solution using a centrifuge and was dried in air.

Powder diffraction was performed using a Bruker D8 diffractometer with Mo-K_α radiation and a Rigaku Miniflex diffractometer with Cu-K_α radiation. Rietveld refinements to X-ray data were performed using Topas 5.

Scanning electron microscopy (SEM) was performed using a JEOL 6060LV with energy dispersive X-ray spectroscopy (EDS). Optical spectroscopy was performed in diffuse reflectance geometry with a Cary 5000 UV-VIS-NIR spectrometer. C,H,N analysis was performed using an Exeter Analytical CE 440.

3.3 Results and Discussion

When $K_2Sn_3O_7$ is placed in water, a new phase is observed. This phase is produced slowly at room temperature, but its formation rate is increased when the water is heated to a steady boil. A systematic study was performed to optimize the amount of time for which the sample was in the water and drying conditions. The most phase-pure and crystalline sample was obtained by placing the $K_2Sn_3O_7$ in boiling water for 1 hour, centrifuging to obtain the solid product, and letting the sample air dry. Since the product is formed readily in water without heating, the phase formed is likely either a hydrated form of $K_2Sn_3O_7$ or a phase where K ions have leached out of the large channel structure that are present in the $K_2Sn_3O_7$ structure.

X-ray diffraction of the new product, shown in Figure 3.1, cannot be fit by any other potassium tin oxide, hydrate, or hydroxide and is distinct from the starting $K_2Sn_3O_7$ precursor. The diffraction experiment was performed using a Cu-Kα source in order to separate the closely packed peaks within the pattern. With less peak overlap, a more accurate peak indexing could be performed. The peaks were indexed to the $P2_12_12$ space group, where a=15.0135(8) Å, b=15.4272(7) Å, and c=3.1022(2) Å. A Le Bail fit to the diffraction pattern is shown in Figure 3.1. This structure is similar to $K_2Sn_3O_7$. Both structures are

Table 3.1: C,H,N analysis results for new phase, noted here as sample RM634C, and other known potassium stannate compounds.

Sample	Theory (wt%)	Run 1 (wt%)	Run 2 (wt%)
$K_2Sn(OH)_6$	2.02	2.05	2.15
K_2SnO_3	0	0.54	0.50
$K_2Sn_3O_7$	0	0.38	0.35
RM634C	?	0.62	0.61

orthorhombic with one short axis of just over 3 Å.

SEM investigation of the new phase, shown in Figure 3.2, reveals that the particles formed are comprised of micron-sized rods. The microstructure of the new phase is very similar to that of the starting material $K_2Sn_3O_7$, shown in Chapter 2. EDS analysis was performed by comparing the spectra from this new compound to that of $K_2Sn_3O_7$ and $K_2Sn(OH)_6$. Since these known compounds have a well defined stoichiometry, the K:Sn ratio of the new compound can be determined with a higher degree of confidence. EDS was also performed on impure samples that still contained $K_2Sn_3O_7$İn these samples two distinct sets of EDS spectra were observed. This shows that the new compound created is not a hydrated $K_2Sn_3O_7$ compound or a polymorph of $K_2Sn_3O_7$ as there are two distinct K:Sn ratios present. The composition of this new compound was measured have a K:Sn ratio around 1:2 which is consistent with a possible $K_2Sn_4O_9$ stoichiometry.

Since the new phase forms readily in water, it is important to characterize the hydrogen content within the new phase to determine if it is an oxide or if the bulk contains hydrogen. C,H,N analysis on the new phases shows an elevated weight percent of hydrogen. However, when compared to other known oxides as standards, the weight percent is similar. The C,H,N results shown in Table 3.1 are not enough to confirm the presence of hydrogen within the bulk of the material as a surface hydroxide could also be present. Further studies, particularly neutron diffraction studies, must be done to determine whether or not the hydrogen is present within the bulk structure of the material.

UV-Vis spectroscopy was performed on the compound to determine how the band gap differs between the starting $K_2Sn_3O_7$ phase and the new compound that was formed. There

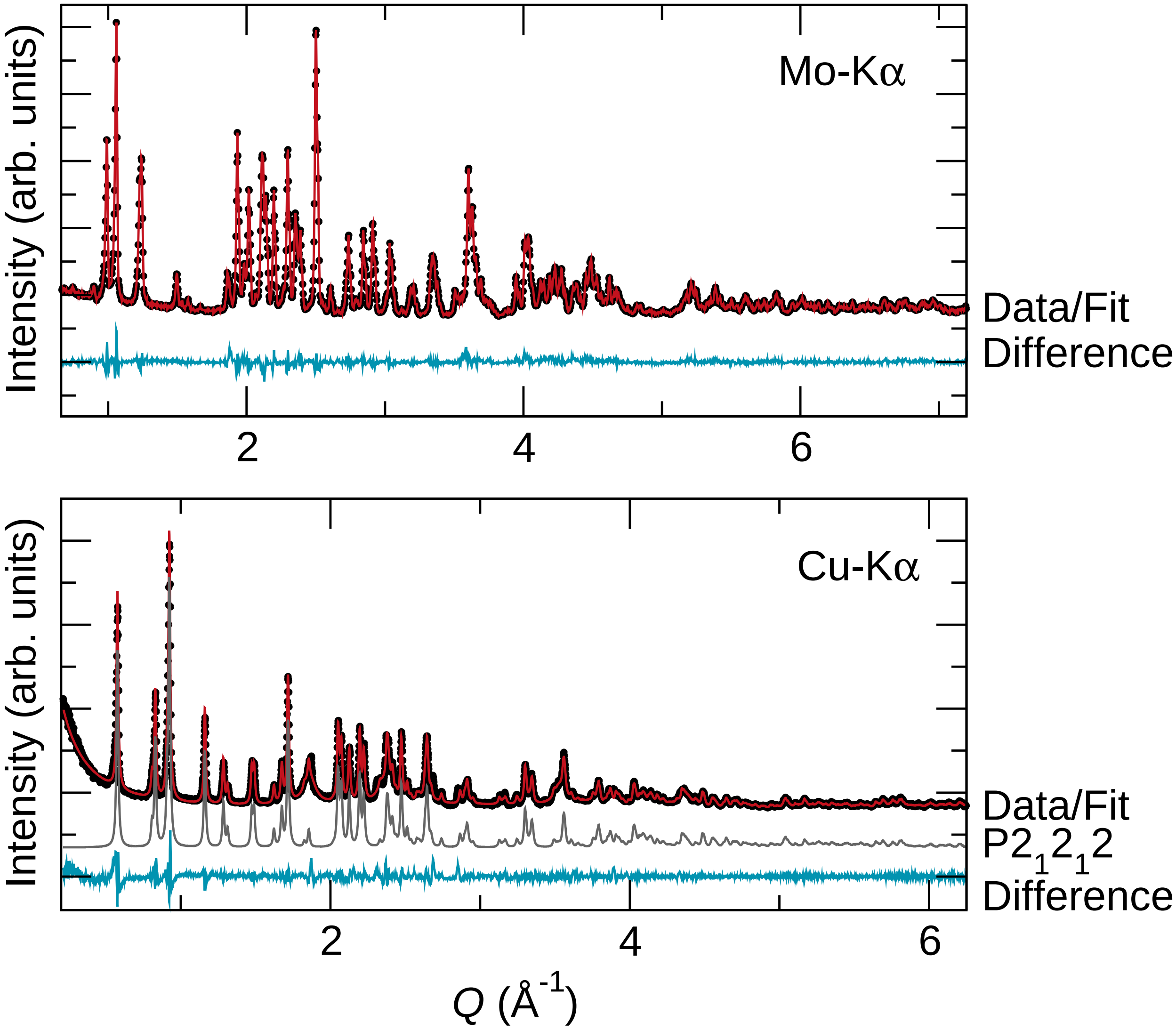

Figure 3.1: Rietveld refinements to starting $K_2Sn_3O_7$ precursor (top) and Le Bail fit to a possible $K_2Sn_4O_9$ unit cell (bottom). Le Bail fit is shown in grey since excess SnO_2 is present in $K_2Sn_4O_9$ sample.

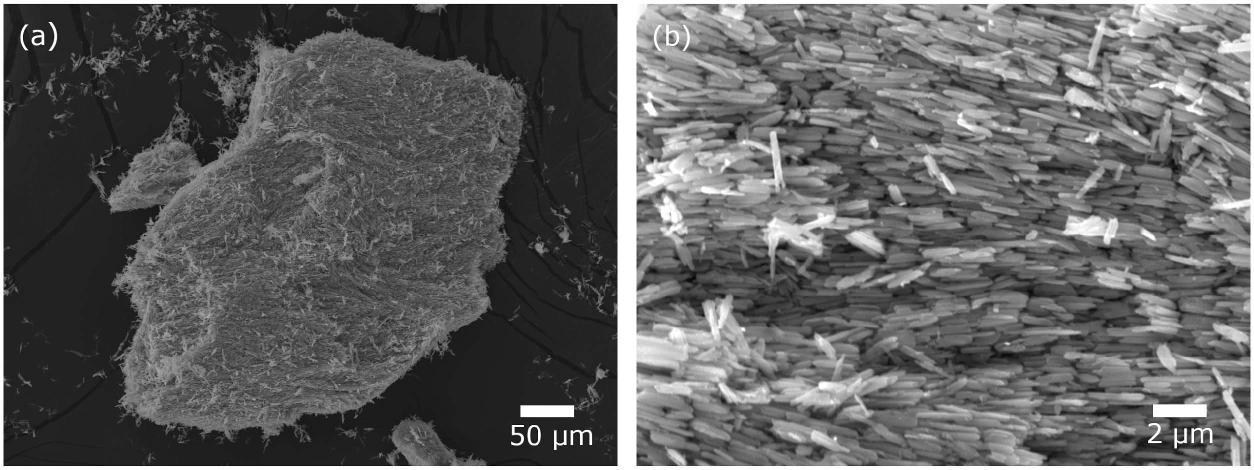

Figure 3.2: Scanning electron micrographs in secondary electron imaging show that (a) particles are formed that are (b) comprised of micron-sized rods.

is a wide transition in both materials. However, the $K_2Sn_4O_9$ compound shows a sharper decrease in reflectivity, whereas $K_2Sn_3O_7$ has a gradual decrease in reflectivity over a large energy range before its downward turn at 3.5 eV.

3.4 Conclusion

A new structure was created upon placing $K_2Sn_3O_7$ in water. Since the new compound is formed readily in water without heating, the structure is likely to be related to the starting $K_2Sn_3O_7$ structure. The cell has been indexed to the $P2_12_12$ space group with a unit cell of a=15.0135(8) Å, b=15.4272(7) Å, and c=3.1022(2) Å. The structure was too complex to be solved using laboratory X-ray diffraction alone. UV-Vis spectroscopy shows a wide band gap of approximately 3 eV with a sharper transition than that of the initial $K_2Sn_3O_7$ structure.

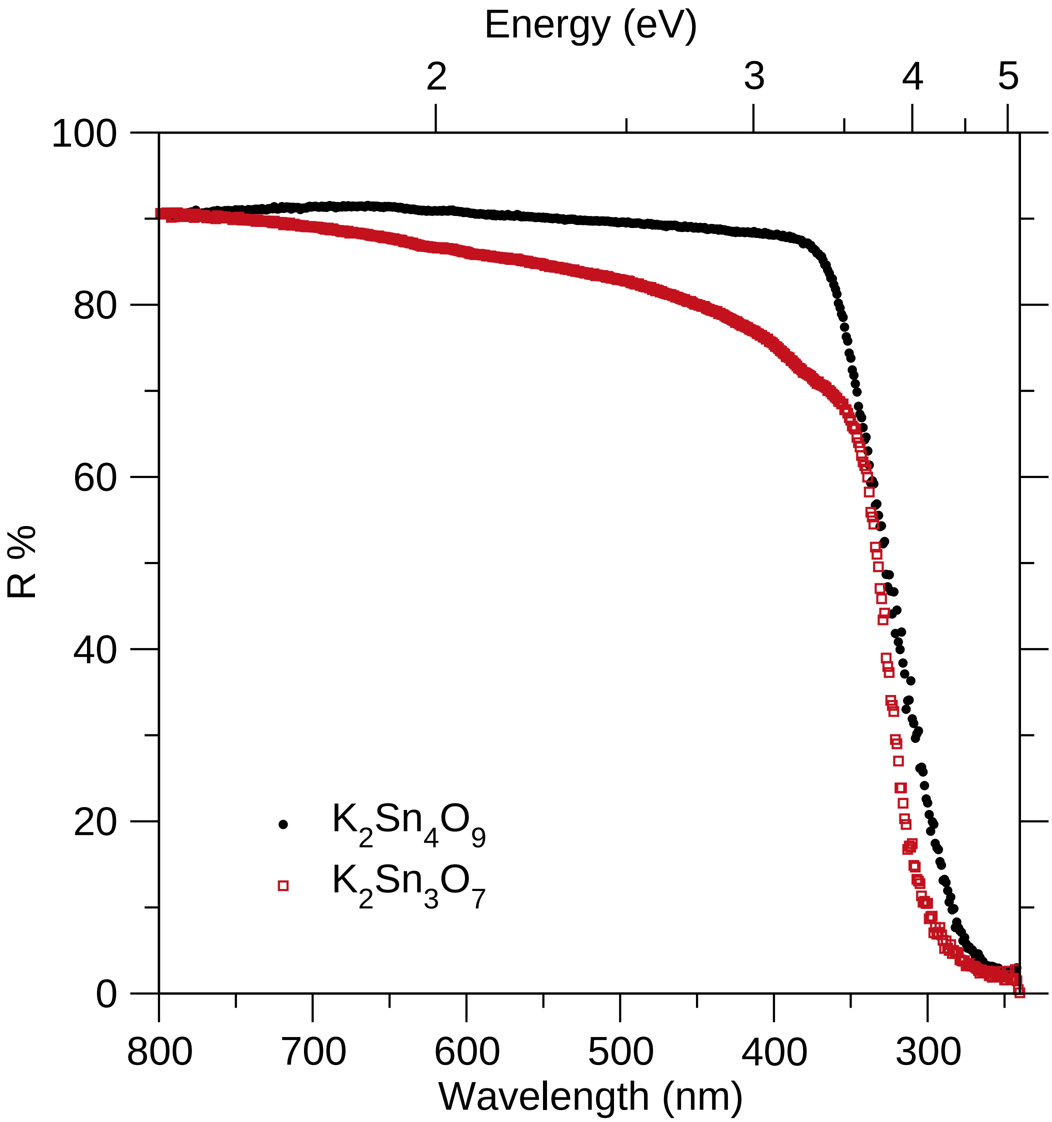

Figure 3.3: UV-Vis spectroscopy of powdered $K_2Sn_4O_9$ and $K_2Sn_3O_7$ both show a large band gap, approximately of 3 eV. $K_2Sn_4O_9$ has a more abrupt change in reflectivity as compared to $K_2Sn_3O_7$

CHAPTER 4

DEVELOPMENT AND CHARACTERIZATION OF IN SITU FLOW CELL

4.1 Introduction

In situ synthesis utilizes a time-resolved characterization technique to monitor the formation of compounds throughout the reaction process. This technique not only gives information about the phases that are formed and their synthesis conditions, but it also provides information about reaction kinetics. In situ synthesis is a valuable method to discover new phases, as transient or metastable phases can be observed. The synthesis conditions for these new phases can then be extracted and used to isolate the new phases ex situ.

In situ heating reactions have been used to understand reaction kinetics and discover new compounds by heating samples of a fixed composition and analyzing the reaction as it proceeds.[50, 51, 52] In situ heating can be combined with additional synthesis techniques to access a larger region of phase space. This combination of techniques is highlighted by the Iversen group with the combination of in situ XRD with solvothermal and high pressure techniques to observe the formation of nanoparticles.[53, 54]

In situ reduction reactions are used to study systems in which specific oxidation states are metastable. In the case of vanadium oxides, in situ reduction reactions allowed for the observation of metastable phases at pure or mixed valences.[55] Metastable phases were stabilized and metal-insulator transitions were determined. In situ synthesis in a reducing atmosphere allows for the controlled synthesis of metastable compounds and can be used to probe a complex phase space.

By creating an in situ cell for studying non-ambient sample environments, phase space can be probed more efficiently. The cell that is discussed in this section can accommodate a wide range of gas atmospheres for reactions up to 1000°C. This cell is also used with a laboratory diffractometer in order to provide a rapid method for exploring compositional space without requiring synchrotron X-ray diffraction.

4.2 In situ cell design

In order to perform reduction reactions at elevated temperatures in an X-ray diffractometer, an in situ cell is needed that can heat a sample while flowing gas in a transmission geometry.

While reduction reactions have been studied in reflection geometry, it is often not feasible.[56] Many flow cells designed for X-ray diffraction in a reflection geometry are made by placing a weakly scattering dome over the sample and heating a platinum strip under the sample. In this type of design, hydrogen reacts with the cell at elevated temperatures. The temperature and gas concentrations experienced by the sample are not well defined in this reflection geometry.[57]

For these reasons, the cell that was developed for the studies presented in this thesis was modeled after an in situ cell design made by Chupas and collaborators that is used at several national laboratories.[58] The cell was modified to be used in a Bruker D8 Advance diffractometer using a Mo X-ray tube and is shown in Figure 4.1.

4.2.1 X-ray flow cell

The flow cell was machined out of 316 stainless steel which was chosen for its corrosion resistance and low chemical reactivity. The design is comprised of two blocks that are separated by two $\frac{1}{4}$" diameter rods. These rods can be secured using set screws and provide flexibility in the capillary length used.

The first block, on the gas inlet side, is mounted to the goniometer by two screws. This block consists of a 3x3 grid of $\frac{1}{4}$" holes, where the top center hole extends halfway through

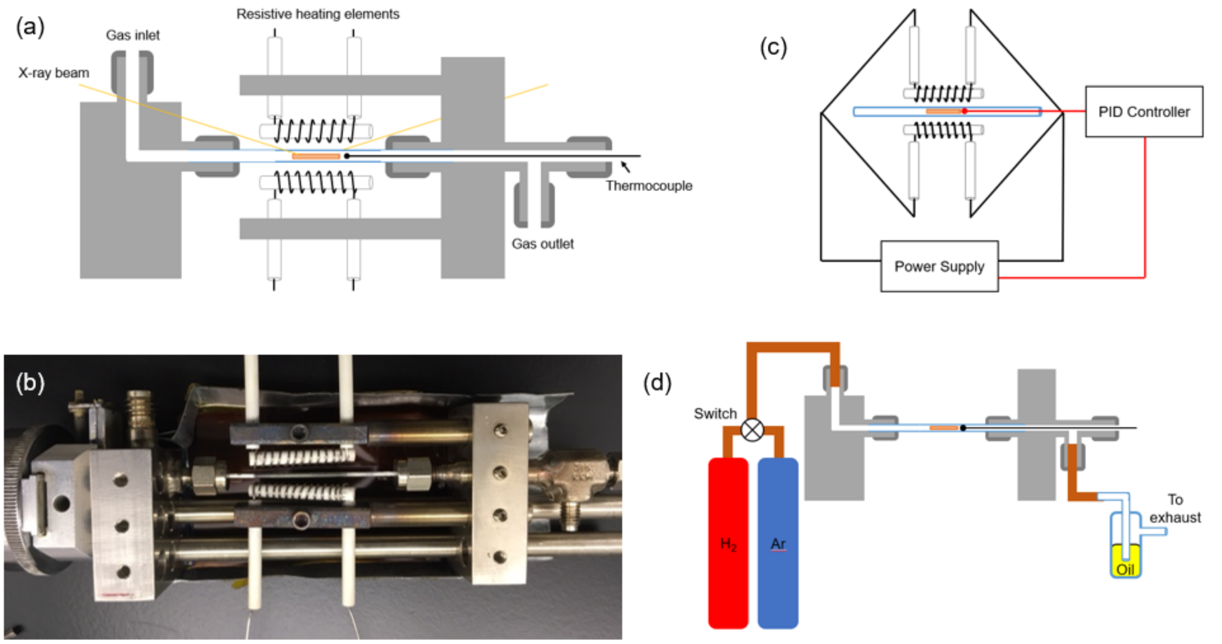

Figure 4.1: Schematic of the in situ flow cell showing (a) the overall design of the cell (b) a photo of the fully assembled cell connected to the goniometer (c) the electrical connections of that control the cell heating and (d) the gas flow setup.

the block and the rest are through holes. Another hole extends from the top of the block to the top center hole in the grid. A $\frac{1}{8}$" Swagelok was welded into the top of the block to connect to the gas line and a 1/16" Swagelok was welded into the front of the block to connect to the sample capillary.

The second block, on the gas outlet side, consists of a 4x2 grid of $\frac{1}{4}$" holes. A T-shaped $\frac{1}{16}$" Swagelok with an elongated branch is used so that the assembly can be held in one of the $\frac{1}{4}$" holes with a set screw. The three branches of the Swagelok assembly go to the capillary, thermocouple inlet, and gas outlet. A schematic and photo of the fully assembled flow cell are shown in Figure 4.1 (a) and (b) respectively.

4.2.2 Temperature control

The sample is heated using two resistive coils. The coils are made of Kanthal wire which has a working temperature up to 1050°C. The Kanthal wire is wrapped around a ceramic rod and the ends run through a hole bored into two other ceramic rods. To achieve uniform heating, the coils should have the same number of turns on the top and bottom, and their spacings should be as uniform as possible. The heating coils are mounted on modified $\frac{1}{4}$" diameter rods that are secured into the block using set screws. The modified rods clamp the ceramic rods to hold them in place without cracking them.

The coils will heat when current is passed through them. The coils are connected in parallel to reduce the total resistance of the system. The reduction in resistance was needed in order to keep the total power supplied at high temperatures within the possible power output of the power supply. At a temperature of 800°C, approximately 175W are supplied by the temperature controller which is 20% of the maximum power of the power supply. The applied voltage is regulated by a temperature controller that is connected to the thermocouple placed within the sample. The temperature controller uses a PID system that adjusts the voltage applied based on the actual sample temperature from the thermocouple. The signal from the temperature controller, which ranges from 0-5 V, is then amplified through the 30V/30A power supply.

Care must be taken to place the thermocouple within the sample and in the heating zone. If the thermocouple is outside of the heating zone, it will read a temperature that is lower than the actual sample temperature. This will cause the temperature controller to send more current to the sample so that the thermocouple reads the desired temperature and will cause overheating of the sample. Alternatively, if the thermocouple is placed too far into the sample, X-rays will diffract off of the thermocouple leading to extra peaks within the diffraction pattern. An internal standard can be placed within the sample to monitor the actual temperature of the sample. This setup is shown in Figure 4.1 (c).

4.2.3 Gas flow control

In this cell, gas flows from a cylinder through a $\frac{1}{8}$" gas line to the capillary and from the capillary through a bubbler with a scrubbing solution and out through the exhaust. The type of gas lines and scrubbing solution must be selected based on their compatibility with the gases and reactions that are being studied. For example, if anhydrous ammonia is used, the gas lines would be stainless steel with dilute sulfuric acid as a scrubbing solution.

For the studies outlined in this document, two gas cylinders, Ar and 5% H_2/Ar, are placed outside of the diffractometer. Copper gas lines are taken from each cylinder into a manual switch. The switch combines the two copper lines and runs through the diffractometer to the gas inlet on the flow cell. The outlet of the flow cell is connected to another stainless steel pipe that connects to a bubbler filled with mineral oil and goes out to exhaust. This setup is shown in Figure 4.1 (d).

4.3 In situ reduction of Mn_3O_4

The gas flow system was first tested on the reduction of Mn_3O_4 because it is easily reduced in hydrogen. The sample was placed in a quartz capillary and X-ray diffraction patterns were collected continuously with each scan lasting 5.5 minutes. An example of a refined X-ray diffraction pattern is shown in Figure X. The sample was heated in Ar to 400°C. Once at 400°C, the gas was switched from Ar to 5% H_2/Ar to reduce the sample isothermally. Immediately after the gases were switched, MnO peaks were observed. After 80 minutes, the sample was completely reduced from Mn_3O_4 to MnO. The gas was then switched back to Ar on cooling to room temperature. The refined weight percents of Mn_3O_4 and MnO throughout the reaction can be seen in Figure 4.3. Now that the reduction of Mn_3O_4 was successfully observed, further reduction studies could be performed.

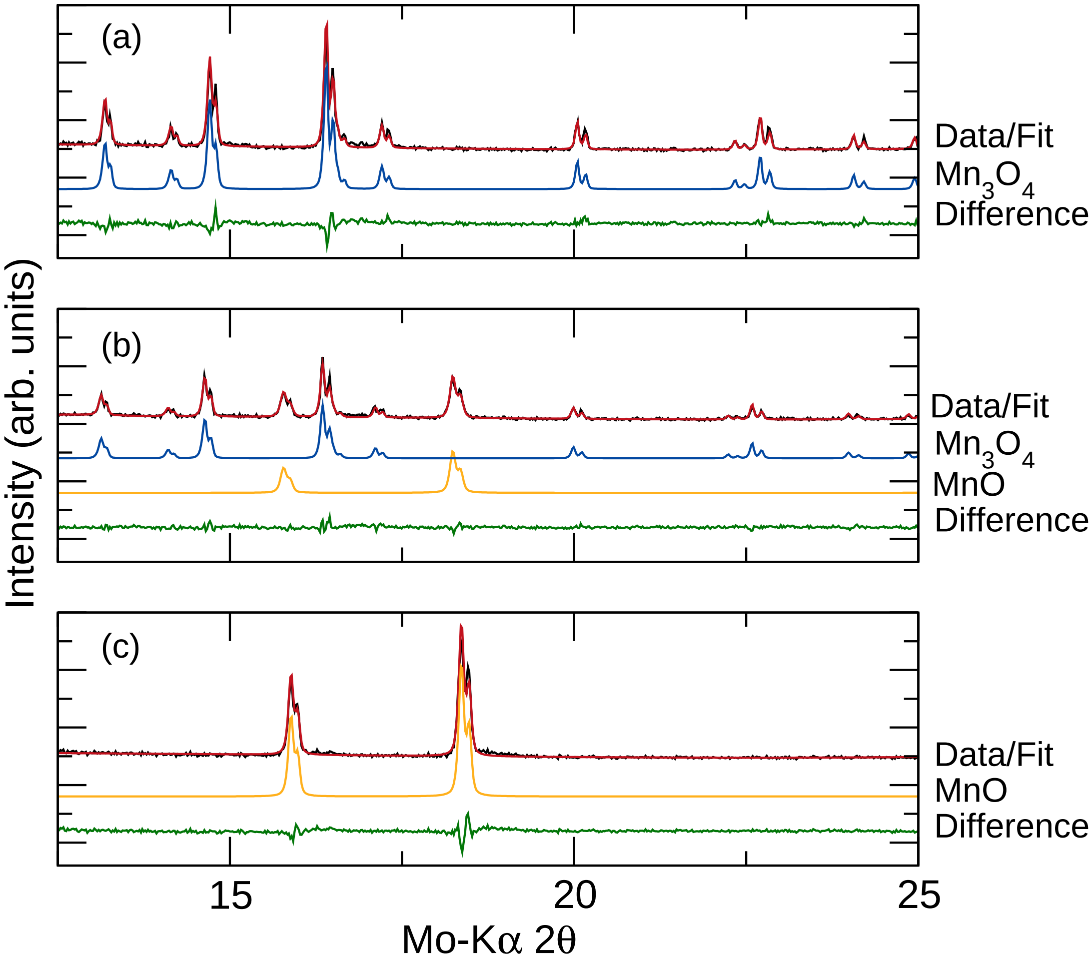

Figure 4.2: Rietveld refinements of three X-ray diffraction patterns from the reduction of Mn_3O_4 to MnO. They show (a) the initial pure Mn_3O_4 phase, (b) the partially reduced state with both Mn_3O_4 and MnO phases, and (c) the final MnO phases

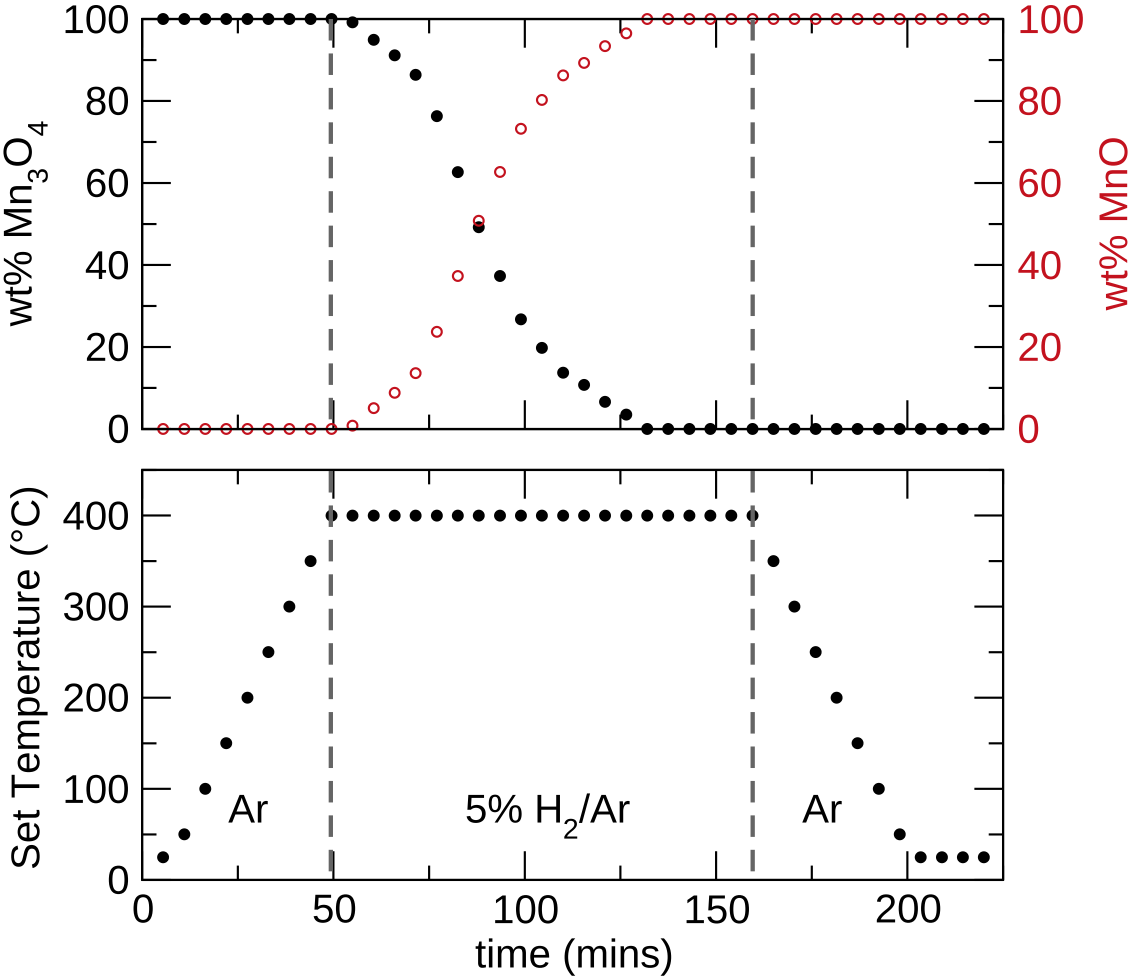

Figure 4.3: Rietveld refinement results of Mn_3O_4 reduction showing the change in wt% of Mn_3O_4 throughout reaction (top) and the set temperature profile (bottom)

CHAPTER 5

HIGH-RESOLUTION AND IN SITU REDUCTION OF FeS_2

5.1 Introduction

Iron pyrite, FeS_2, is a potential photovoltaic absorbing material that exhibits several promising properties, such as high quantum efficiency,[60, 61] high absorption coefficient,[62] and a band gap of 0.95 eV.[63, 62, 64, 60, 65] Pyrite is also earth-abundant and non-toxic making it a cost-effective alternative, especially in contrast to In-, Ga-, and Cd-containing compounds.[60, 66] Despite these advantages, high dark currents due to low open-circuit voltages limit device efficiencies and have prevented the demonstration of a viable pyrite-based solar cell.[62, 61]

Three reasons can be invoked to explain the limited efficiency of pyrite: phase equilibria, surface effects, and intrinsic defects. These issues are not mutually exclusive. The first problem of phase equilibria is the most straightforward to probe. Any presence of magnetic, metallic pyrrhotite $Fe_{1-\delta}S$ precludes uniform semiconducting behavior.[67, 68, 69] Synthesis or annealing with sulfur overpressure seems to eliminate pyrrhotite and any amorphous sulfur-deficient phases.[70, 69, 71, 72]

The second problem of surface effects has been investigated computationally.[73, 74, 75] Several investigations into the formation of defects along the lowest energy surface, the (100) plane, have shown that the formation energy of sulfur vacancies decreases when moved from

---

Reproduced from reference [59] with permission of the International Union of Crystallography the bulk to the surface. This can create surface states within the band gap, lowering the band gap from 0.95 to 0.34 eV.[76] Studies have also found that samples annealed in a sulfur-rich environment, which could prevent the formation of sulfur-deficient phases, can also form a metallic sulfur-rich surface layer that decreases the open circuit voltage, limiting the material for photovoltaic applications.[77]

The third problem, that of intrinsic defects, has also received recent computational treatment. Density functional theory studies have reached a consensus that intrinsic defects in pyrite, such as sulfur vacancies, V_S, have relatively high formation energies, on the order of 2-3.5 eV.[78, 72, 79, 76, 80] The concentration of sulfur vacancies at synthesis temperatures should be below 10^{14} cm^{-3}, with the caveats noted by Hu that oxides often display many vacancies with supposed high formation enthalpies and that the charge states of defects in pyrite are not established.[78] So, it is perhaps not surprising that the reported defect concentrations would vary from 10^{20} to $< 10^{10}$ cm^{-3}.[81, 82]

Here high-resolution and in situ X-ray diffraction (XRD) is used to monitor the lattice parameter of FeS_2 and the formation of secondary phases in order to rule out pervasive bulk defects in FeS_2. However, this characterization requires careful analysis and standardization.

Pyrite has the cubic $Pa\overline{3}$ structure, shown in Figure 5.1, and can be described as an NaCl analog with Fe^{2+} cations and S_2^{2-} anions.[83] Over 50 compounds adopt the MX_2 pyrite structure.[84, 85] Many are considered to be line compounds, such as CoS_2 and CuS_2.[86] While there are examples of non-stoichiometric structures, notably $NiS_{2-\delta}$, these structures are thought to have variable metal concentrations with stable anion concentrations.[87]

The synthetic techniques that have historically produced pyrite must be considered when investigating its intrinsic stoichiometry range. These techniques include chemical vapor transport (CVT),[62, 61, 88, 64, 81, 89, 71] metalorganic chemical vapor deposition (MOCVD), [90, 91] sulfurization of iron and iron oxides,[92, 93, 94, 95, 96, 97, 98, 68, 99] solvothermal synthesis,[100, 101, 102, 103] flux growth, [104] electrodeposition,[105] and solid-state methods.[106] Crucially, some of these studies into pyrite stoichiometry, such as those per-

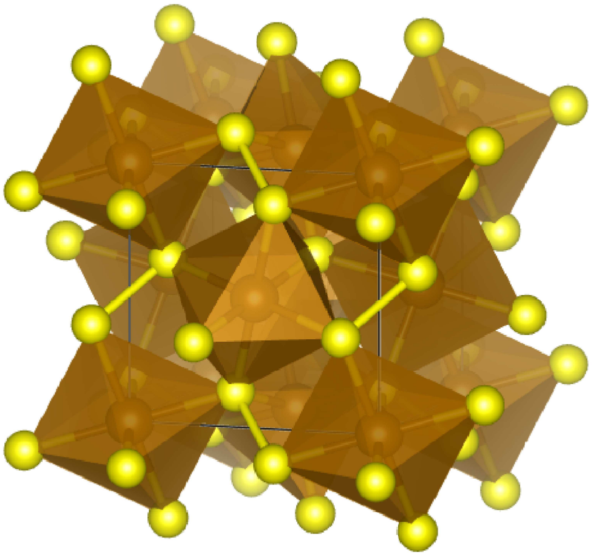

Figure 5.1: Crystal structure of pyrite FeS_2 showing Fe^{2+} cations on an fcc sublattice and S_2^{2-} dimers. Reproduced from reference [59] with permission of the International Union of Crystallography

formed by Nakamura, Birkholz, and Reijnen, include carrier gases or additives that can incorporate into the pyrite lattice and convolute studies of its intrinsic behavior.[81, 91, 105] The solid-state methods used here avoid inclusion of foreign elements.

Several different Fe-S phase diagrams are used that depict different thermodynamic behaviors versus temperature. Some show FeS_2 as a line compound,[106] while others show FeS_2 with a stoichiometry range of $FeS_{2-\delta}$, where δ ranges from 0.05 to 0.25.[89] In this study, in situ XRD is utilized to map the extent of non-stoichiometry in FeS_2. By performing in situ XRD experiments in a reducing atmosphere, the stoichiometry range of FeS_2 can be fully investigated.

5.2 Methods

Iron sulfide powders were synthesized from elemental Fe (Alfa, 99%) and S (Alfa, 99.5%). Iron powder purity was verified to be greater than 99.8% by X-ray fluorescence (XRF) with a Shimadzu EDX-700 energy-dispersive X-ray fluorescence spectrometer. Sulfur powder was purified three times prior to use through a sublimation process. Sublimation was performed by placing sulfur into a sealed and evacuated quartz ampoule with a 120° bend in the middle. The side of the tube with sulfur was placed in the hot zone of a tube furnace which was tilted at a 30° angle and preheated to 400°C. The other end of the tube remained outside of the furnace to create a cold zone for the sulfur to condense. The black, hydrocarbon-containing impurities remained in the hot end of the tube for the first two runs.

Pyrite samples were synthesized by mixing Fe and S powders together in nominal compositions of FeS_x, where $1.90 \leq x \leq 2.25$. The powders were mixed under argon using an agate mortar and pestle, then loaded into 15 mm diameter quartz tubes, and sealed under vacuum. The tubes were heated for 24 hours at 600°C with heating and cooling rates of 10°C/min.

High-resolution ex situ synchrotron powder XRD was performed on vacuum-sealed samples at the 11-BM beamline at the Advanced Photon Source (APS) using 30 keV X-rays ($\lambda = 0.414621$ or 0.414167 Å, calibrated by Si in two separate batches of runs).

High-temperature in situ powder XRD was performed using a Bruker D8 Advance diffractometer using a Mo-Kα source. The samples that were used in the high temperature diffraction experiments were synthesized with nominal excess-sulfur stoichiometry $FeS_{2.25}$ and were mixed with 30 wt% MgO powder (Strem Chemicals, 99.5%) to monitor the sample temperature. The heating and cooling rates were 5°C/min.

In situ reduction experiments were performed in a resistively-heated capillary flow cell where the mounted samples were placed in an open-ended 1 mm diameter fused silica capillary.[58] The flow cell system was purged with Ar gas for one hour prior to heating. Argon was passed over the sample during heating and cooling. Upon equilibration at 400°C, 5% H_2/Ar flow was initiated at approximately 60 sccm. In situ heating experiments were performed using samples sealed inside of a 0.7 mm diameter fused silica capillary that was placed inside an unsealed 1 mm capillary. A scan time of 1244 seconds (~20 minutes) was used for each in situ XRD pattern. Rietveld refinements were performed using TOPAS 5.

Crystal structures were visualized using VESTA.[107]

5.3 Results and Discussion

5.3.1 High-resolution diffraction of the claimed stoichiometry range

Samples were prepared with nominal stoichiometries from $FeS_{1.9}$ to $FeS_{2.25}$. If the stoichiometry were to vary across the range of sulfur content, as in TiS_2, the lattice constants should change linearly with respect to anion occupancy due to Vergard's law in the single phase regime.[108, 109] These large concentrations of vacancies, as claimed by Birkholz, should be observable, especially in high-resolution data, as demonstrated by Lussier's study on oxygen content in $YPrO_{3-\delta}$.[81, 110] On the other hand, no deviations in lattice parameter or relative peak intensities would be observed for a line compound—rather, the appearance of new secondary phases would signal crossing from the FeS_2 + S to the FeS_2 + $Fe_{1-\delta}S$ two-phase region.

High-resolution, ex situ XRD was used to determine the structure of pyrite on the S-poor and S-rich sides of its stability range. As seen in Figure 5.2, due to the extremely high signal-to-noise ratio in synchrotron XRD data, secondary phases are able to be observed at all nominal stoichiometries. A transition from sulfur-poor to sulfur-rich secondary phases is observed between the nominal stoichiometries of $FeS_{2.1}$ (Fe_7S_8-containing) and $FeS_{2.15}$ (S_8-containing). The presence of marcasite, an FeS2 polymorph, can be ruled out in all samples since its no additional peaks corresponding to the phase are observed. [111, 112]

While this transition occurs at a nominal sulfur-to-iron ratio larger than 2, some sulfur vapor pressure is inevitable at the processing temperature of 600°C and deposits on the walls of the ampoule upon cooling. This deposition of sulfur necessitates a slight excess of sulfur for bulk synthesis to obtain a sample with FeS_2 stoichiometry.

The refined FeS_2 lattice parameter (a), and $8a$ sulfur position, (u, u, u), obtained using Rietveld refinement are shown in Table 5.1. For each nominal stoichiometry, the sulfur

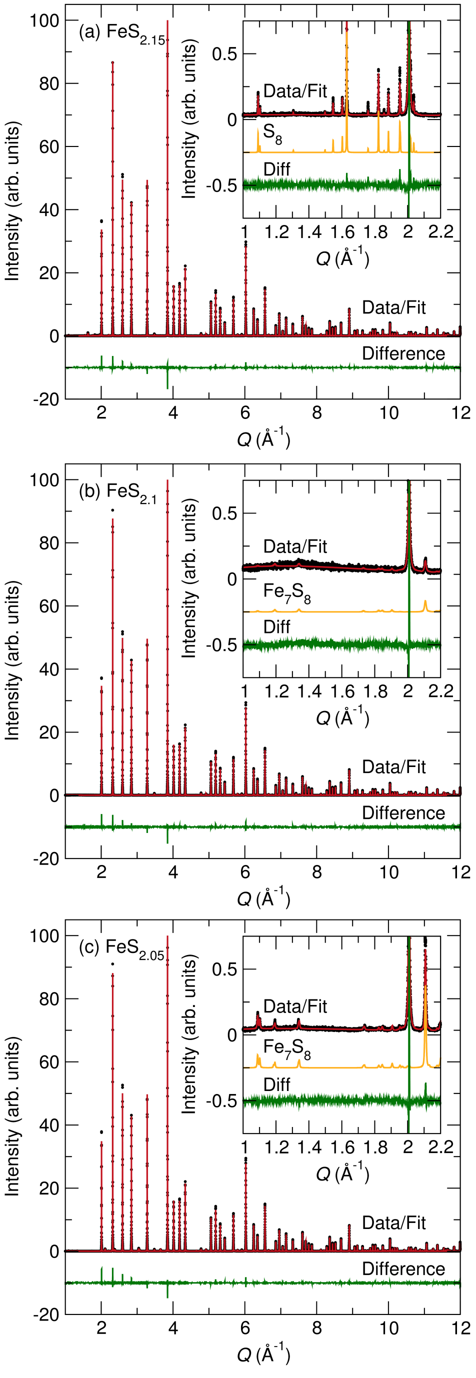

Figure 5.2: Rietveld refinement of 11-BM data for samples that span the pyrite Fe:S ratio. The most phase pure sample was synthesized at a nominal sulfur content of 2.1, which is higher than the stoichiometric value of 2. Excess sulfur is present in samples with a higher sulfur content than 2.1 and Fe_7S_8 is present in samples with a lower S content. Reproduced from reference [59] with permission of the International Union of Crystallography

Table 5.1: Structural parameters for FeS_2 obtained from Rietveld refinement of high-resolution X-ray diffraction patterns from 11-BM. S:Fe ratios shown are nominal values. Reproduced from reference [59] with permission of the International Union of Crystallography

S:Fe Ratio	a (Å)	u	R_{wp}
1.9	5.418026(4)	0.38475(3)	11.650
1.92	5.418030(2)	0.384733(19)	8.147
1.94	5.418017(3)	0.38475(2)	9.792
1.96	5.418067(3)	0.38477(2)	9.754
1.98	5.418035(3)	0.38478(3)	9.947
2	5.418053(3)	0.38473(2)	9.488
2.05	5.4179979(19)	0.384781(18)	8.179
2.1	5.4179922(19)	0.384773(18)	8.373
2.15	5.4180053(17)	0.384787(16)	7.823
2.2	5.4180516(18)	0.384756(17)	7.565

occupancy values were able to be refined and FeS_2 in each sample was determined to be of stoichiometric composition within 0.0075%. The sulfur occupancy was also refined allowing for oxygen alloying on the sulfur site in case of contamination, and no change in occupancy was observed. The goodness of fit is shown to increase as the nominal stoichiometry decreases due the fit of sulfur-poor phase, Fe_7S_8. As the amount of Fe_7S_8 increases, R_{wp} value also increases. Fe_7S_8 is difficult to fit due to its large number of ordered defect structures and small wt% within the sample.

The lattice parameter of the pyrite FeS_2 phase from the data in this study, as well as other previously published works, is shown in Figure 5.3. The standard deviation, σ, in the refined lattice parameters is 2.5×10^{-5} Å for nominal stoichiometries of FeS_x where $1.90 \leq x \leq 2.2$. There is *no statistically significant change in the pyrite lattice parameter* between the S-rich and S-poor (Fe_7S_8-containing) samples. Within the limits of ex situ synchrotron diffraction, pyrite prepared with autogeneous sulfur pressure behaves like a line compound.

5.3.2 Comparison to previous studies

The most notable studies of the experimental pyrite stoichiometry are those of Birkholz, Fiechter, and de las Heras[81, 89, 92]. Their findings are summarized in Table 5.2 and those with lattice parameters are plotted alongside this studies in Figure 5.3. Table 5.2 outlines the proposed defects and characterization techniques of similar studies as well. The first section of this table highlights studies that specifically study sulfur vacancies in FeS_2, while the subsequent sections highlight other defects observed in FeS_2. Here, the findings of this study are critically compared with those of the three most relevant studies.

Studies 1 & 2: Birkholz, 1991 and Fiechter, 1992.

In CVT growth studies by Birkholz and Fietcher, crystals of "$FeS_{2-\delta}$" were grown using a Br_2 transport agent. These crystals were crushed and analyzed using powder XRD, induced coupled plasma atomic emission spectroscopy (ICP-AES), pycnometry, and transmission electron microscopy. While many cite these studies to show that $FeS_{2-\delta}$ has a stoichiometry range from $\delta = 0.05$ to 0.25,[92, 113, 114] this study is in agreement with those of Yu, Berry, and Ellmer which state that this stoichiometry range is smaller than previously reported and the percentage of sulfur vacancies in the lattice is most likely $\leq 1\%$.[72, 115, 116]

The lattice parameters in these studies were determined using laboratory XRD with whole pattern refinements, however no standard material was included to quantify or reduce systematic errors. These lattice parameters for these CVD samples have a total spread of 4×10^{-4} Å for a S:Fe ratio ranging from 1.75 to 2.05. The S:Fe ratio of these materials was determined using refinements of laboratory XRD by Birkholz while Fiechter also utilized ICP-AES and coulometric measurements.

Relying on standardless laboratory XRD data to determine precise lattice parameters and site occupancy without a standard is unreliable, and doping on sulfur sites by bromine would convolute with the noise in the measurement. Luck used ICP-AES to show that cystals grown by Fiechter using CVT methods had Br impurities from the transport agent

(30-280 μg/g) and P impurities from the sulfur source (170-210 μg/g).[117] Electron spin resonance measurements performed by Siebert determined Br will create Br–S bonds in the FeS_2 lattice.[118]. Hu calculated that these Br–S bonds act as an n-type dopant in the lattice.[78] Phosphorus has also been observed occupying the S site in similar compounds.[117] If Br or P were to occupy the S site, this could explain the decrease in the sulfur content observed using ICP-AES.

Study 3: de las Heras, 1995.

In this study, iron films on glass substrates were sulfidized at different sulfur pressures and temperatures. The resulting film were between 430 and 700 nm thick.[92] The lattice parameter and sulfur occupancy were *refined simultaneously* to laboratory Cu-Kα XRD data. The reported occupancy in particular is dubious since the refinement is only fit to nine low-intensity peaks, when additional degrees of freedom include the sulfur position, u, and at least two atomic displacement parameters. The stochiometries and their errors were not confirmed by other methods. Large deviations in reported lattice parameters at the same claimed S:Fe ratio are additional signs that systemic errors may dominate the stoichiometry determination.

In the study by de las Heras, samples were synthesized at various temperatures and sulfur vapor pressures, so it is crucial to determine whether the S content in pyrite is fixed (as it appears in the ex situ data) or flexible as a function of S partial pressure.

This study.

The high purity of the samples (containing Fe and S only) in this study is supported by ex situ refinements and purification of S precursors. No evidence of oxide phases or deviations in S occupancy were present in any of the high-resolution 11-BM diffraction patterns, as seen in Figure 5.2 and Table 5.1.

High-resolution XRD provides the most precise lattice parameters, and accuracy is ensured

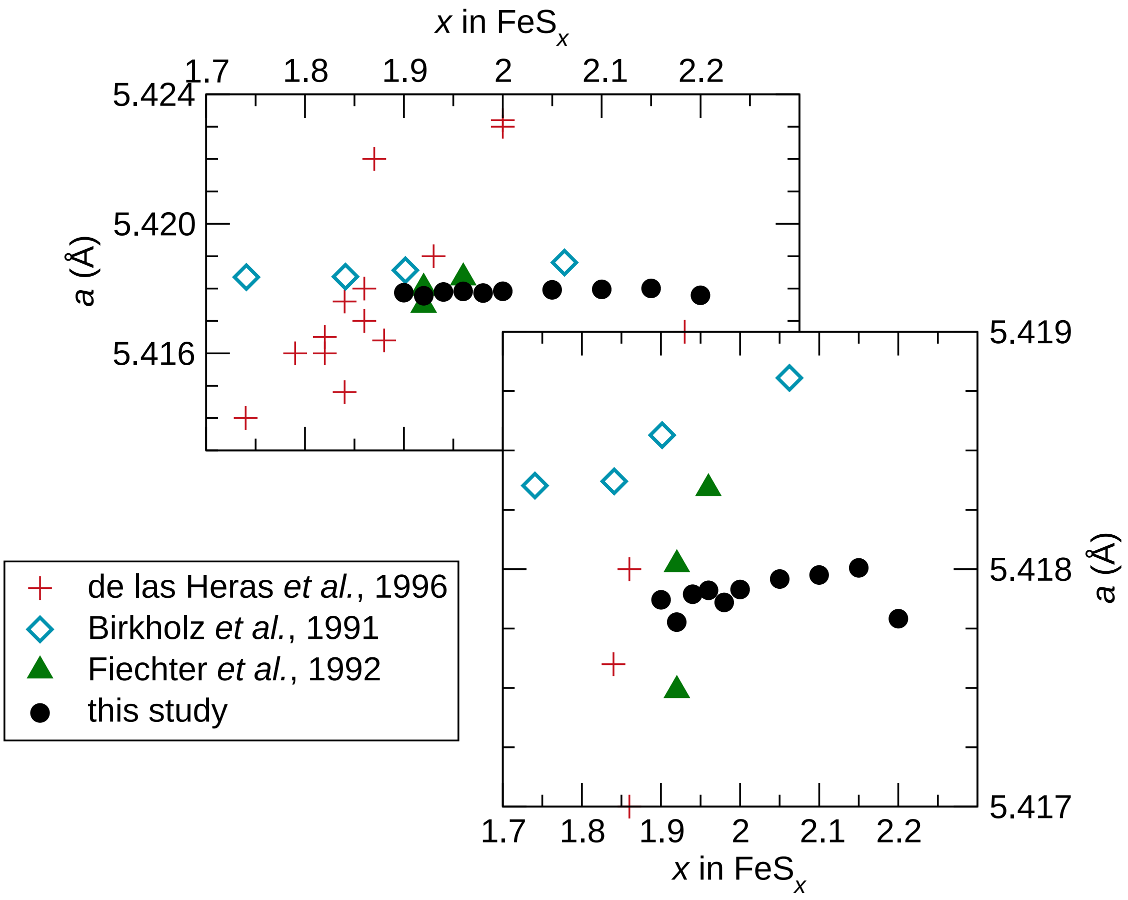

Figure 5.3: Comparison of pyrite lattice parameters from multiple studies. The graph shows that the refined 11-BM lattice parameters in this study show a smaller change over the nominal stoichiometry range as compared to previous studies. Reproduced from reference [59] with permission of the International Union of Crystallography

by calibration using a Si standard for each set of runs. This study shows no evidence of lattice parameter deviations larger than $\sigma = 2\times10^{-4}$ Å and instead points to other defects, such as the formation of secondary phases, as the primary defect when synthesizing FeS_2.

Comparison to similar compounds.

Some pyrite-structure compounds display intrinsic non-stoichiometry (NiS_2 and $CoSe_2$), but they are exceptions to the rule.[87, 119] The ex situ deviations in lattice parameter are vanishingly small in comparison to those of a flexible pyrite, $NiS_{2-\delta}$, and non-stoichiometric $Fe_{1-\delta}S$ (Figure 5.4). $NiS_{2-\delta}$ shows a 1.3×10^{-2} Å difference in lattice parameter over a 10%

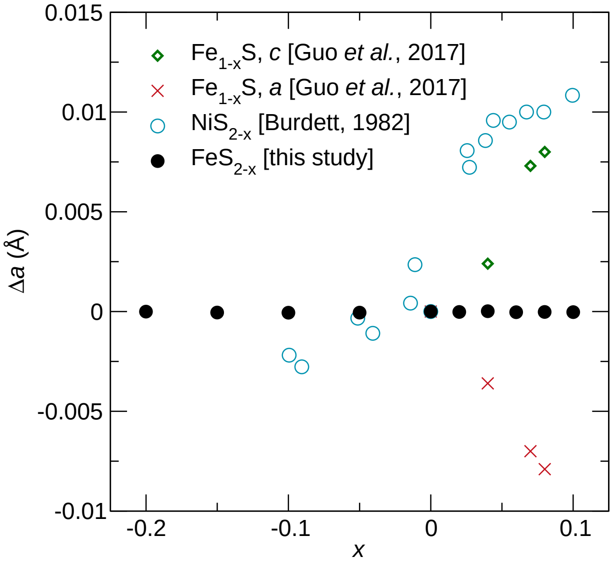

Figure 5.4: Comparison of deviations in lattice parameters of non-stoichiometric $NiS_{2-\delta}$ and $Fe_{1-\delta}S$. The graph shows the change in lattice parameter with respect to the lattice parameter measured at the stoichiometric composition (x=0). The FeS_2 data from this study shows practically no change over the nominal stoichiometry range as compared with other similar compounds. Reproduced from reference [59] with permission of the International Union of Crystallography

sulfur range.[87] $Fe_{1-\delta}S$ shows a 8×10^{-3} Å difference for a 0.8% decrease in iron content.[120] Existing claims about pyrite only show a contraction of 4×10^{-4} Å for a reported 13% decrease in sulfur content.[81]

The spread in lattice parameter for pyrite $NiS_{2-\delta}$ is two orders of magnitude larger than the changes observed in the ex situ synchrotron work in this study, as well as the previous studies by Birkholz and Fietcher which claimed to be seeing a comparable change in stoichiometry.[81, 89] From this vantage point, the intrinsic FeS_2 stoichiometry range is very narrow. If one assumes that the relationship between lattice parameter and stoichiometry in FeS_2 is similar to that of $NiS_{2-\delta}$, then a deviation in lattice parameter of 2×10^{-4} Å sets a ceiling on sulfur deficiency around 0.02% (200 ppm).

Table 5.2: Overview of previously published literature results on the synthesis of FeS_2 highlighting the defect model, synthesis method, characterization techniques used, and the purpose of the paper that presented the work. Reproduced from reference [59] with permission of the International Union of Crystallography

Proposed Defect	Synthesis	Characterization	Purpose of Study	Citation
Non-stoichiometry due to sulfur vacancies				
Sulfur vacancies	CVT - Br	ICP-AES, XRD	Stoichiometry of FeS_2	[81]
Sulfur vacancies	CVT - Br	XRD, Density, TEM	Stoichiometry of FeS_2	[89]
Sulfur vacancies	Iron sulfidation	XRD	Thin film microstructure	[92]
Common defects in CVT growth				
Sulfur vacancies, Br incorporation	CVT - Br	ICP-MS, ICP-AES	Purity of synthetic FeS_2 crystals	[117]
Br incorporation	CVT - Br	ESR	Effect of transport agent	[118]
Common defects in thin film growth				
Sulfur interstitials, iron vacancies	Steel Sulfidation	XRD, Raman	Nanowire growth	[121]
C,H,O incorporation, marcasite impurity	APCVD	XRD, Raman, Auger, SIMS, RBS, XPS	Thin film growth	[115]
Marcasite impurity	Thermal Sulfidation	Raman	Thin film growth	[67]
$Fe_{1-x}S$ impurity	Thermal Sulfidation	WAXRD, Raman, EDS	Thin film stoichiometry	[69]

5.3.3 In situ reduction of FeS_2

The ex situ studies above show that pyrite prepared at a specific condition (600°C, vacuum) behaves as a line compound. Ex situ work, however, does not address the behavior of defects at elevated temperatures. Sulfur vacancies that are formed at elevated temperatures may recombine with sulfur vapor on cooling, creating an appearance of FeS_2 as a line compound. In situ reduction reactions allow us to probe the temperature dependence of vacancy formation.

In order to determine whether FeS_2 could be sulfur-rich at elevated temperatures, in situ heating experiments in the presence of excess sulfur in a sealed capillary were performed. If excess sulfur is present in the structure, one would expect an expansion of the FeS_2 lattice to accommodate the excess sulfur. This study began with a sample with a nominal stoichiometry of $FeS_{2.25}$, which has even more excess crystalline sulfur present than the $FeS_{2.15}$ sample in Figure 2(a). The sample was heated in a sealed capillary to 400°C with excess sulfur present; no change of the FeS_2 lattice parameter was observed, as seen in Figure 5.5. The standard deviation, σ, of the FeS_2 lattice parameter is 7.6×10^{-5} Å for the diffraction patterns collected at 400°C.

Next, this study investigated the lower bound on sulfur content within FeS_2. If FeS_2 is a line compound with a fixed stoichiometry, there should be no observable change in the pyrite lattice parameter during isothermal reduction from S-rich to S-poor. If single-phase FeS_2 has a significant compositional width due to sulfur vacancies, the lattice parameter should change upon reduction. This behavior is shown in the oxidation of defect perovskites, such as $SrCoO_{2.5+\delta}$. [122]

The in situ reduction reaction was performed using a sample with a nominal stoichiometry of $FeS_{2.25}$ at 300°C and 400°C. The diffraction patterns from a reduction run performed at 400°C are shown in Figure 5.6. The sample was ramped (under Ar) to 400°C and held for four scans ($\sim$ 80 minutes) to ensure equilibration. Reduction by 5% H_2/Ar showed that sulfur-poor Fe_7S_8 (marked by asterisks) begins to form within the first 40 minutes of H_2 flow.

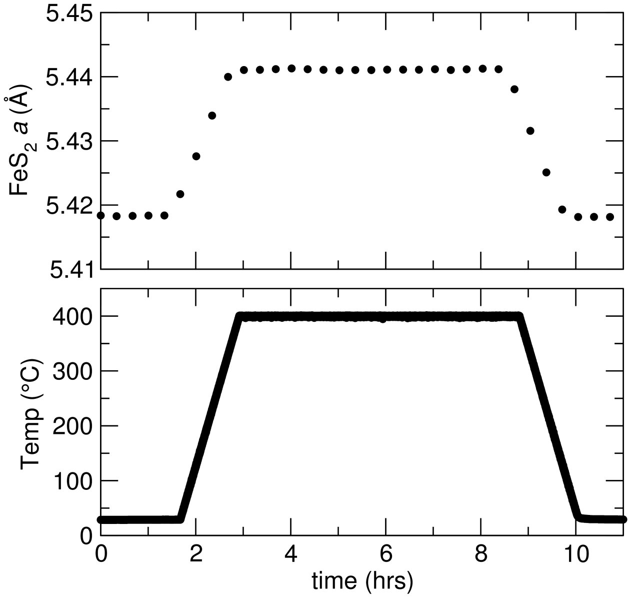

Figure 5.5: Data from nominal $FeS_{2.25}$ heated in a sealed capillary to 400°C showing (a) refined FeS_2 lattice parameter from Rietveld refinements and (b) average temperature of each measurement. Reproduced from reference [59] with permission of the International Union of Crystallography

Rietveld refinements of the in situ data reveal lattice parameter trends and Fe_7S_8 content shown in Figure 5.7. In this experiment, he formation of sulfur-deficient Fe_7S_8 was observed in conjunction with an apparent contraction in the lattice parameter of 1.91×10^{-3} Å and 2.13×10^{-3} Å for runs at 300°C and 400°C respectively. This contraction is of the same order of magnitude as previously reported non-stoichiometric compounds shown in Figure 5.4.

During the reaction, the lattice parameter of FeS_2 increased and decreased as expected due to thermal expansion. Upon isothermal reduction, Fe_7S_8 appears within the first two scans. As the reduction proceeds, a small lattice parameter change is also observed. While this lattice parameter change could indicate that intrinsic defects are present in the FeS_2 structure, further investigation of the peaks indicates that this shift is most likely due to inhomogeneous strain in the starting material.

It is critical to include a MgO standard to ensure that thermal expansion or drift of the sample during heating is not misinterpreted as lattice contraction or expansion of pyrite. The lattice parameters of the MgO standard were constrained to be constant throughout

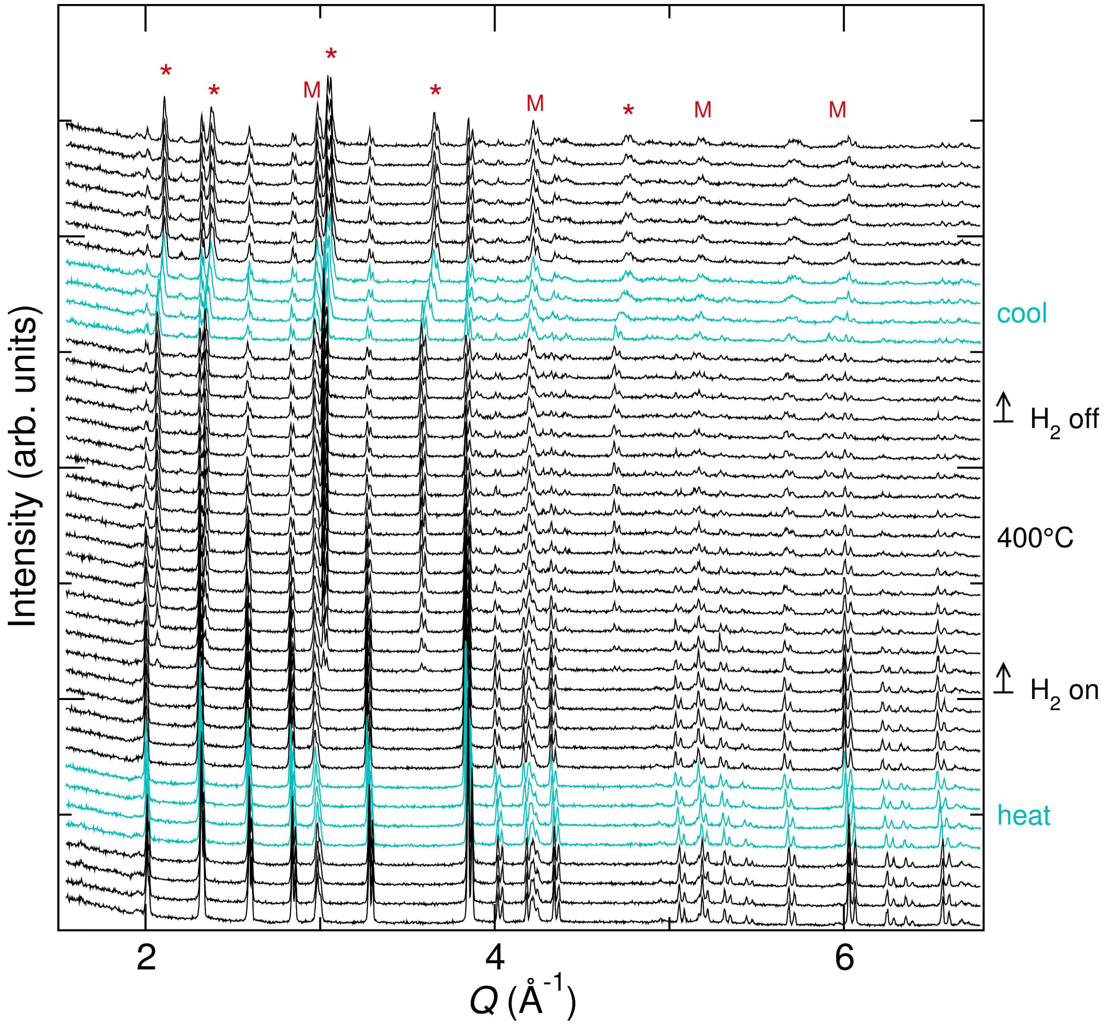

Figure 5.6: Waterfall plot of in situ X-ray diffraction reduction of FeS_2 at 400°C. Lattice parameters are observed to expand and contract on heating and cooling respectively. Sulfur-deficient Fe_7S_8 peaks, denoted by (*), begin to appear after H_2 gas starts to flow. Peaks from the MgO standard, denoted by (M), can be observed throughout the entire reaction. Reproduced from reference [59] with permission of the International Union of Crystallography

the isothermal reduction, while the pyrite lattice parameters were refined in the experiment in Figure 5.7(a). Even with the MgO lattice parameter allowed to refine (Figure 5.7(c)), the apparent contraction of the pyrite lattice is obvious.

To verify the lattice parameter refinement at elevated temperatures, the lattice parameter of FeS_2 was locked to the initial refined value at high temperature and compared to the data at the end of the reduction reaction, still at 400°C. As shown in Figure 5.8(a), the non-refined lattice parameter does not accurately fit the FeS_2 peaks. It is only when the FeS_2 lattice parameter is refined in Figure 5.8(b) that the peaks are properly modeled.

The deviation in lattice parameter during the reduction was 1.91×10^{-3} Å for a 11.3% change in weight percent for FeS_2 at 300°C and 2.13×10^{-3} Å for a 74.9% change in weight percent for FeS_2 at 400°C. The initial and final lattice parameters were obtained from the refinements of long, 1-hour scans taken before and after the reduction process as seen in Figure 5.9.

Does the apparent lattice contraction in lattice parameters in Figure 5.7(a) mean that pyrite begins to host sulfur vacancies as it is reduced? In fact, no. A closer look at the final and initial diffraction patterns in Figure 5.10 shows that the reduced pyrite peaks never move from the "footprint" of the initial peak. No region of altered stoichiometry is necessarily created. Surface strain or disorder is a more likely explanation for the expanded state of pyrite at the beginning of the reaction. Additionally, one would expect $FeS_{2-\delta}$ to expand during reduction as does $NiS_{2-\delta}$, not contract.

5.4 Conclusions

Studies have shown conflicting views on the extent of non-stoichiometry in FeS_2. Early studies on CVT-grown single crystals claimed that pyrite could have a sulfur deficiency upwards of 12%, while recent computational treatments calculate a maximum vacancy concentration below 10^{14} cm^{-3}. [89, 78] The studies on single crystals, however, had problems with sev-

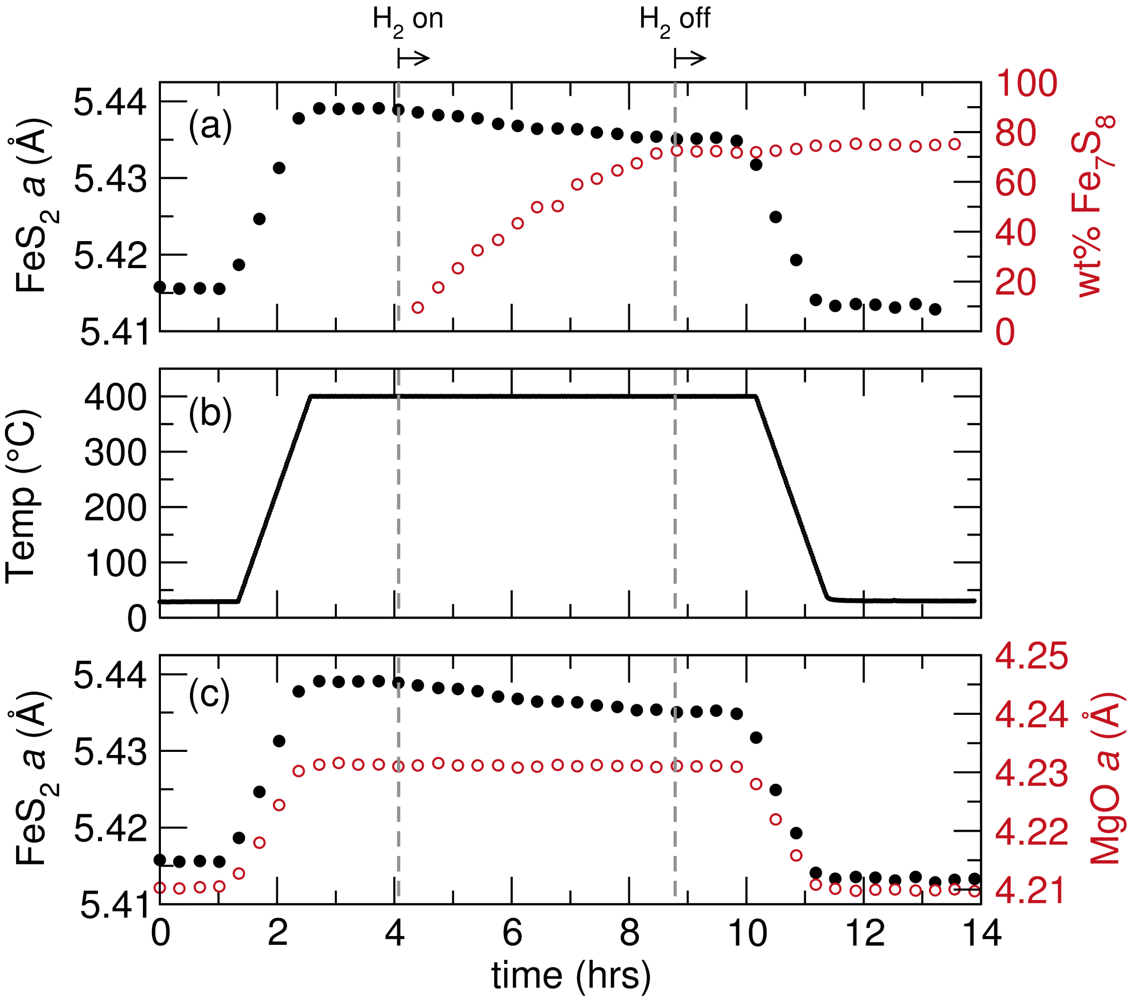

Figure 5.7: Rietveld refinement results of X-ray diffraction reduction data shown in Figure 5.6 with (a) lattice parameters and weight percent with MgO lattice parameters locked, (b) temperature profile of the reaction from the thermocouple throughout the reaction process, and (c) refinement of MgO and FeS_2 lattice parameters. Reproduced from reference [59] with permission of the International Union of Crystallography

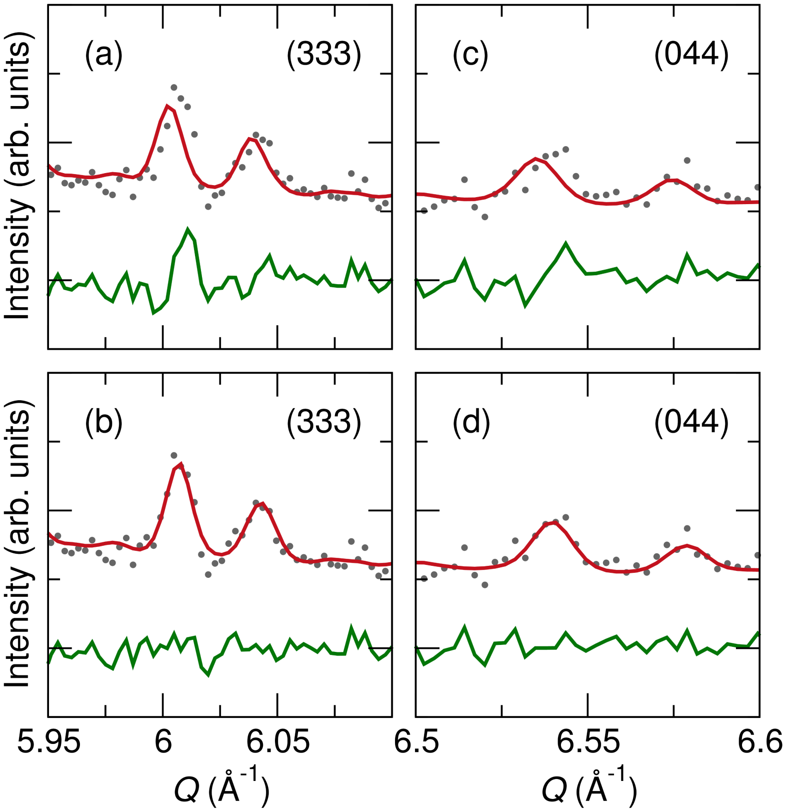

Figure 5.8: Rietveld refinements of the last high temperature pattern in the 400°C reduction with the lattice parameter locked to the initial high temperature value (a, c) and the refined lattice parameter (b, d) for two different high angle peaks. The refinement with the lattice parameter locked shows an offset between the data and the fit. Reproduced from reference [59] with permission of the International Union of Crystallography

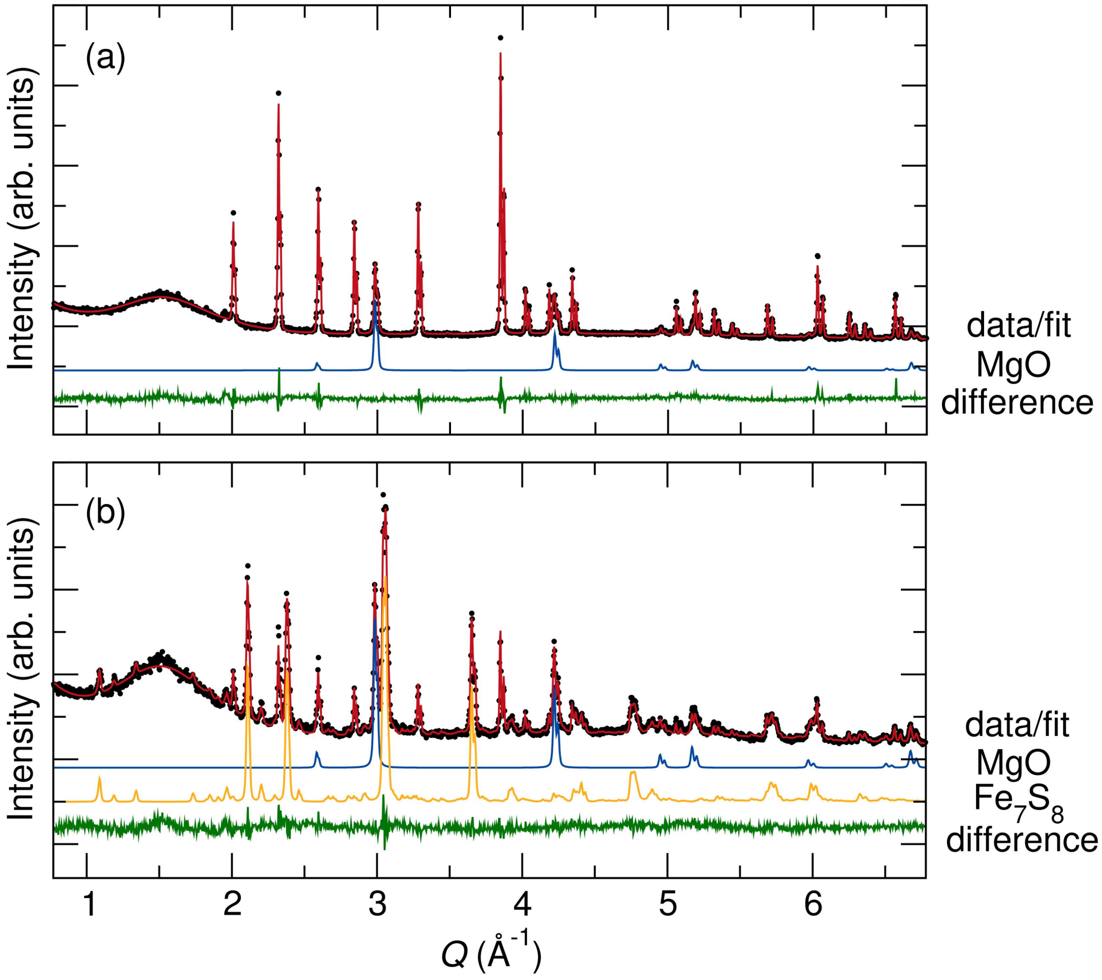

Figure 5.9: Rietveld refinements of pyrite X-ray diffraction patterns with added MgO standard (a) before and (b) after in situ reduction at 400°C. The lattice parameter of FeS_2 contracts by 2.13×10^{-3} Å from 5.41527(10) Å before the reduction to 5.41314(15) Å after the reaction is completed. Reproduced from reference [59] with permission of the International Union of Crystallography

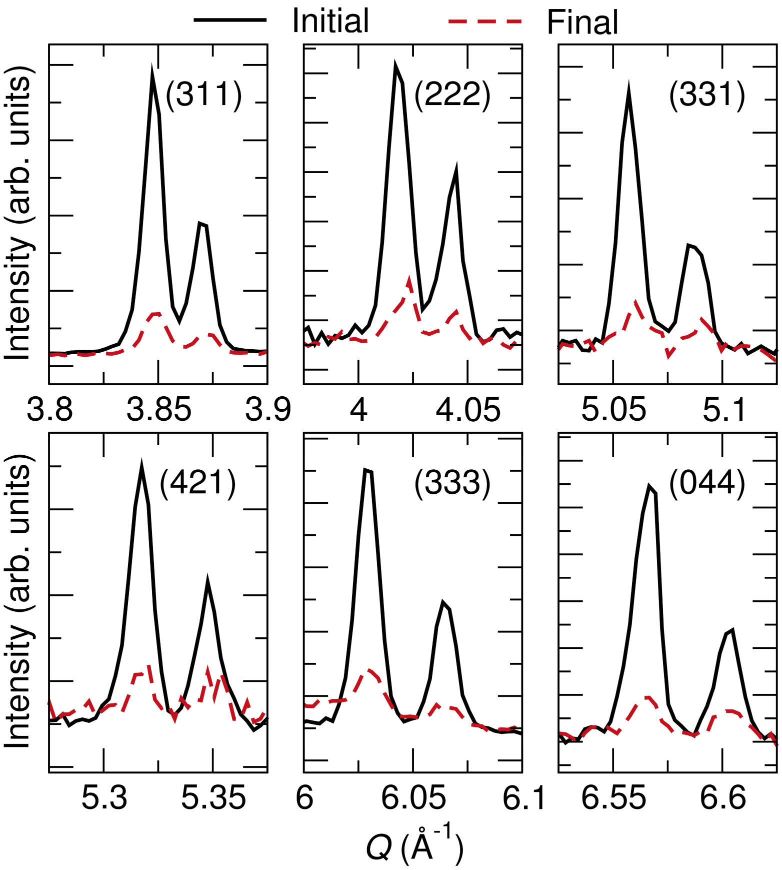

Figure 5.10: Peaks for initial and final scans from 400°C reduction. While the peaks show a slight shift, none of the final peaks separate from their initial peak. This shows that no new regions with a stoichiometry different from the initial sample are created during reduction. Reproduced from reference [59] with permission of the International Union of Crystallography

eral sources of potential contamination that lead to incorrect interpretations of spectroscopy results that gave the illusion of large sulfur deficiency values. The results in this study contradict these studies and do not indicate a large compositional width in FeS_2, and instead put an upper boundary on potential vacancies based on the detection limits of XRD techniques. Our results also more closely resemble recent computational efforts and thin film synthesis work that points to the formation of sulfur-deficient secondary phases with much lower possible concentrations of sulfur vacancies in FeS_2.[78, 69, 70, 72]

Pyrite formed with autogeneous partial pressures of sulfur does not contain enough intrinsic vacancies to be resolved in high-resolution diffraction. Calibration of XRD experiments by using appropriate standards is crucial to determine whether the observed trends arise from the material or from noise. Our study found that a sensitivity greater than 10^{-4} Å would be needed to determine any trends in lattice parameter with relation to defect formation in ex situ data. At this resolution, FeS_2 could have a sulfur vacancy concentration of up to 0.02% when compared to $NiS_{2-\delta}$.

In situ reduction of FeS_2 showed no observable single-phase compositional width present in FeS_2. Instead sulfur-deficient secondary phases were formed almost immediately. While intrinsic defects could still be present, no region of altered stoichiometry was observed. A small compositional window could be observed using a less powerful reducing agent or high-resolution XRD at high-Q values. Other techniques that could be utilized to probe intrinsic defects concentrations below the detection of XRD are secondary ion mass spectroscopy (SIMS) which provides impurity concentrations as a function of depth in the material, X-ray photoelectron spectroscopy (XPS) which shows defects based on surface bonding states, or photoluminescence (PL) which detects low concentrations of defects based on low-temperature spectral peaks associated with specific material impurities.[123, 115, 124]

This study shows that to synthesize pure FeS_2, one of the most important requirements is pure precursor materials. By using solid-state synthesis, purified precursors, and rigorous XRD experiments, sources of contamination were eliminated and sources of experimental error in measurements were minimized. This allowed for more confidence in stoichiometry values obtained from XRD. It was also observed that secondary phase formation can be controlled by synthesizing FeS_2 at autogeneous partial pressures of sulfur.

CHAPTER 6

IN SITU REDUCTION OF K-Sn-O COMPOUNDS

6.1 Introduction

The K-Sn-O phase diagram hosts six ternary phases with known structures. These phases lie on one of two lines between either KO_2 and SnO_2 for Sn^{4+}-containing compounds or KO_2 and SnO for Sn^{2+}-containing compounds. While several phases have been realized on the K-rich side of the phase diagram, no Sn^{2+}-containing compounds have been discovered with a Sn content higher than a 1:1 ratio of K:Sn.

Reducing known compounds provides a synthesis route that could yield more kinetically stable phases. Since precursors do not need to be reacted at high temperatures, reductions can be performed at low temperatures that are not traditionally probed. At these temperatures, oxygen can be slowly removed from the system allowing for the exploration of the phase space below the Sn^{4+} line.

In situ reduction reactions can also be used to explore the phase space in between the Sn^{4+} and Sn^{2+}-containing compounds to explore the possibility of discovering a material with mixed valence tin. While the formation of mixed valence tin oxides is rare and the compounds are metastable, some mixed valence binary tin oxides have been observed.[125]

Here, in situ reduction reactions are performed in an attempt to discover new Sn^{2+} or mixed valence compounds. Reduction reactions are performed on multiple Sn^{4+} phases to explore the empty Sn-rich region of the phase diagram.

6.2 Methods

$K_2Sn_3O_7$ was synthesized using KO_2 and SnO_2 in a molar ratio of 2:3 K:Sn. KO_2 and SnO_2 were ground by hand in an agate mortar and pestle in a N_2 filled glove bag. The mixture was fired in uncovered alumina crucibles at 900°C for 9 hours in a N_2 atmosphere. The mixture was heated in a box furnace with heating and cooling rates of 10°C/min.

In situ reduction experiments were performed in a resistively-heated capillary flow cell where the mounted samples were placed in an open-ended 1 mm diameter fused silica capillary.[58] The flow cell system was purged with Ar gas for one hour prior to heating. Argon was passed over the sample during heating and cooling. Upon equilibration at the max temperature (400 or 500°C), 5% H_2/Ar flow was initiated at approximately 60 sccm. All samples were mixed with 30 wt% MgO as a temperature standard. The X-ray diffraction patterns were measured using Mo-Kα radiation with a 2θ range of 5-31 degrees with a scan time of 920 s.

Rietveld refinements to X-ray data was performed using Topas 5. X-ray diffraction data was plotted with GSAS-II.[126]

6.3 Results and Discussion

6.3.1 In situ reduction of $K_2Sn_3O_7$

$K_2Sn_3O_7$ was placed in a quartz capillary with 30 wt% MgO as a temperature standard. The capillary was reduced in 5% H_2/Ar gas at both 400 and 500°C. No reaction was observed upon heating $K_2Sn_3O_7$ to the max temperature and at both temperatures $K_2Sn_3O_7$ was observed to reduce into $K_2Sn_2O_3$ within the first 15 minutes in the reducing atmosphere. The samples continued to reduce to K_2SnO_3 over time and only 9 wt% remained after 6 hours at 500°C. Upon cooling the capillaries $K_2Sn_3O_7$ persisted to room temperature and metallic Sn crystallized. The contour plot showing the peak intensities over time for the

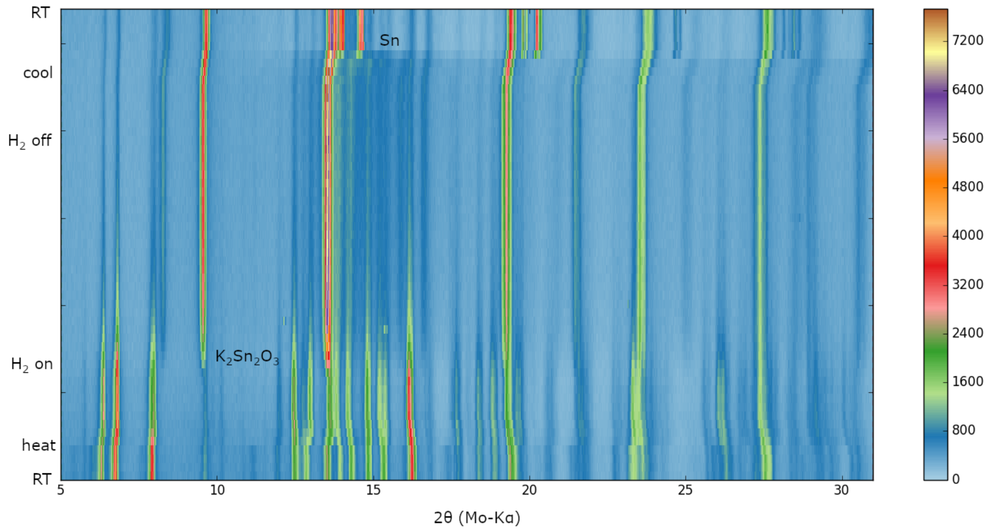

Figure 6.1: Contour plot of X-ray diffraction data from the in situ reduction of $K_2Sn_3O_7$ at 500°C in 5% H_2/Ar gas. Upon reduction in 5% H_2/Ar gas, $K_2Sn_2O_3$ appears increases and $K_2Sn_3O_7$ is reduced. On cooling Sn is observed to crystallize from a molten state.

reduction at 500°C. is shown in Figure 6.1. No new phases were observed to form during the reduction of $K_2Sn_3O_7$, however, this reaction is the first synthesis method to produce $K_2Sn_2O_3$ without the use of K_2O.

Since the K_2SnO_3 almost immediately upon reducing $K_2Sn_3O_7$, it is possible that the a transition period with an intermediary phase could have been missed. If any intermediary phase is present for less than the scan rate, the peaks can be missed since they would only be present for a short period of the total collection time. This problem can be alleviated by either slowing the reaction by changing the reaction temperature or reducing agent or the data could be collected with a 2D detector that would collect the whole diffraction pattern at once rather than scanning through a range of 2θ values. If peaks are observed in part of the diffraction pattern, but a whole pattern cannot be collected, using a 2D detector would be ideal for observing these phases.

In order to slow the reaction in this study, $K_2Sn_3O_7$ was also heated to 400°C in a N_2 atomosphere to deduce if any intermediate phases were formed during the reduction that were not observable because of the quick reduction time when using 5% H_2/Ar gas. No

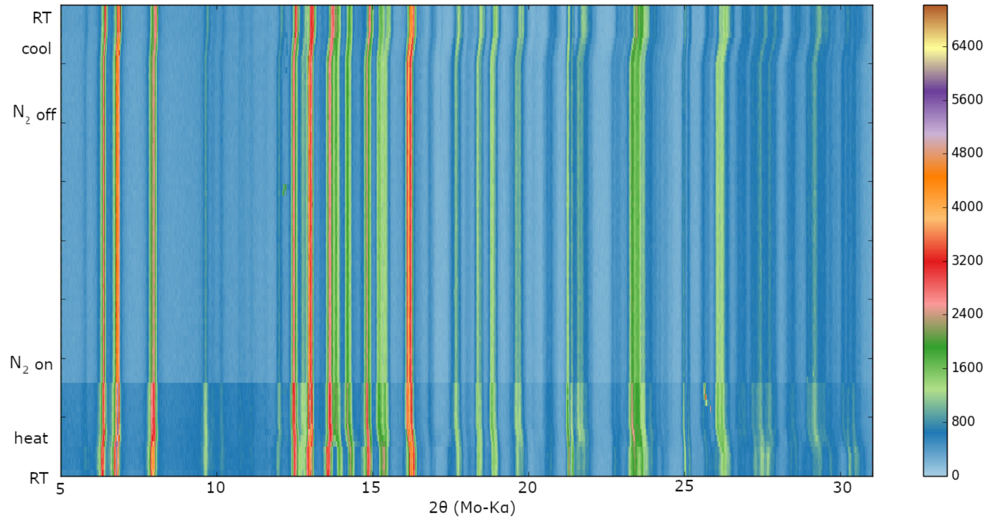

Figure 6.2: Contour plot of X-ray diffraction data from the in situ reduction of $K_2Sn_3O_7$ at 400°C in N_2. No change occurs and $K_2Sn_3O_7$ is present throughout the entire reaction.

changes were observed in the $K_2Sn_3O_7$ sample after 6 hours at 400°C in N_2. The contour plot showing the peak intensities over time for the reaction at 400°C in N_2 is shown in Figure 6.2. It is possible that by using a gas that is less reducing than 5% H_2/Ar but more reducing than N_2 could yield intermediary phases, but no such phases were observed in this study.

6.3.2 In situ reduction of $K_2Sn(OH)_6$

$K_2Sn(OH)_6$ was placed in a quartz capillary with 30 wt% MgO as a temperature standard. No reaction was observed on heating in an Ar atmosphere to 400°C. Once at 400°C, the temperature was held in order to ensure temperature stability before starting the reduction. During this hold at 400°C a new phase was observed. This new pattern could not be refined to any known potassium tin oxides or hydroxides. Upon further investigation, the peaks match a phase, $K_2SnO_3{\cdot}3H_2O$, from a previous study by Tournoux.[9] The investigation of this phase will be discussed further in Chapter 7.

After 1 hour at 400°C, this new phase was observed to reduce into $K_2Sn_2O_3$ within the first 15 minutes in the reducing atmosphere. Once again the amount of $K_2Sn_2O_3$ increased

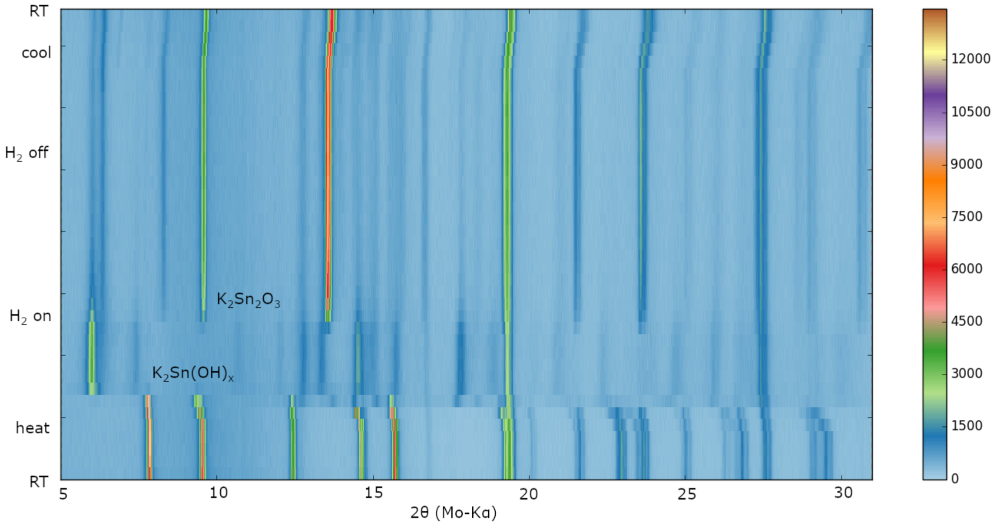

Figure 6.3: Contour plot of X-ray diffraction data from the in situ reduction of $K_2Sn(OH)_6$ at 400°C. Upon reaching 400°C, $K_2Sn(OH)_6$ disappears and a new phase is formed. When this phase is reduced in 5% H_2/Ar gas, $K_2Sn_2O_3$ appears and persists for the remainder of the reaction.

with reduction time. Since the reduction forms $K_2Sn_2O_3$, a potassium-rich phase should also be observed upon reduction. It is possible that this phase may not be observed due to the formation KOH that is being removed with the gas flow during the reduction process. The contour plot showing the peak intensities over time for the reduction at 400°C. is shown in Figure 6.3.

6.4 Conclusion

Two different Sn^{4+}-containing compounds were reduced in 5% H_2/Ar gas using the in situ gas flow cell discussed in Chapter 5. These compounds were chosen to investigate the empty phase space for tin-rich Sn^{2+}-containing compounds. This study did not show any evidence of new Sn^{2+}-containing compounds in this region of the phase diagram. However, the synthesis conditions of a new phase that was created on heating $K_2Sn(OH)_6$ were determined.

While no new phases were realized, this study shows an effective, rapid search of phase space. Each in situ reaction was performed over the course of approximately 12 hours in a laboratory environment. By utilizing in situ characterization in carefully chosen material systems, effective high-throughput materials discovery can be performed.

CHAPTER 7

DECOMPOSITION OF $K_2Sn(OH)_6$

7.1 Introduction

$K_2Sn(OH)_6$, often referred to as $K_2SnO_3{\cdot}3H_2O$, is frequently used as a reactant to synthesize Sn-based compounds, such as nanoparticles and hollow SnO_2 spheres because of its high solubility in water at a wide range of compositions.[127, 128, 129] .

While the structure of $K_2Sn(OH)_6$ has been investigated and refined, relatively few studies have discussed other potassium stannate hydroxides.[130] Initial results on the decomposition of $K_2Sn(OH)_6$ were noted by Tournoux in his studies of the K-Sn-O system. Tournoux highlighted two decomposition phases which he referred to as $3K_2SnO_2{\cdot}2H_2O$ and $K_2SnO_3{\cdot}H_2O$, but did not provide crystal structures for either phase.[9] These two compounds were noted to form as $K_2Sn(OH)_6$ was heated in either vacuum or a nitrogen atomsphere. The noted compositions were based on the amount of weight loss on heating rather than the potential structures that were formed.[9]

Here, a study of the decomposition $K_2Sn(OH)_6$ is performed and the structure of the new phase, referred to as $K_2Sn(OH)_x$ is investigated.

7.2 Methods

$K_2Sn(OH)_x$ and K_2SnO_3 were synthesized by firing $K_2Sn(OH)_6$ that was ground in an agate mortar and pestle. Both samples were fired in uncovered alumina crucibles in a N_2 atmosphere within a box furnace. $K_2Sn(OH)_x$ was fired at 400°C for 1 minute with heating and cooling rates of 5°C/min and K_2SnO_3 was fired at 600°C for 9 hours with heating and cooling rates of 10°C/min.

Rietveld refinements to X-ray data was performed using Topas 5.

Fourier transform infared (FTIR) spectroscopy was performed with a Nicolet Nexus 670 FTIR. C,H,N analysis was performed using a Exeter Analytical CE 440.

7.3 Results and Discussion

7.3.1 Decomposition of $K_2Sn(OH)_6$ in N_2

In Chapter 6, a new phase was observed by heating $K_2Sn(OH)_6$ to 400°C in an inert atmosphere. These synthesis conditions were used to isolate the new phase, $K_2Sn(OH)_x$, ex situ. After a systematic set of experiments were performed with a range of reaction times, it was found that heating $K_2Sn(OH)_6$ to 400°C and holding for one minute in a N_2 atmosphere yielded the purest sample containing only the desired new phase.

In order to further study the phases formed by heating $K_2Sn(OH)_6$ in an inert atmosphere, the reaction time at 400°C was increased. The formation of $K_2Sn(OH)_6$ increases with reaction time. It should be noted that the reaction is also reversible. When placed at room temperature in air, K_2SnO_3 will transform back to $K_2Sn(OH)_6$ over the course of a couple hours.

7.3.2 Investigation of intermediate phase

$K_2Sn(OH)_x$ has not been previously investigated. From the decomposition reaction, a K:Sn ratio of 2:1 must be maintained throughout the formation of the secondary phase. This ratio would be consistent with the prediction by Tournoux that the phase is $3K_2SnO_2 \cdot 2H_2O$, however, since the starting material is a hydroxide it would be more likely that the secondary phase is also a hydroxide compound rather than a hydrate.[9]

Table 7.1: C,H,N analysis results for the weight percent of hydrogen within each sample. Two batches of the intermediary phase were analyzed and are compared with other known materials.

Sample	Theory (wt%)	Run 1 (wt%)	Run 2 (wt%)
$K_2Sn(OH)_6$	2.02	2.05	2.15
K_2SnO_3	0	0.54	0.50
$K_2Sn_3O_7$	0	0.38	0.35
RM642	?	0.89	0.91
RM641	?	0.81	0.81

X-ray diffraction was performed on the powder of the new phase to confirm that no known impurity phases were present. The diffraction pattern was indexed to the P222 space group with a unit cell of a=13.518(2) Å, b=6.1699(7) Å, and c=9.3973(12) Å. The structure can be similarly indexed to the C222 space group as well. A Le Bail fit to the indexed cell is shown in Figure 7.1

C,H,N anaylsis was performed to determine the weight percent of hydrogen within the sample. The results from two pure batches, RM641 amd RM642, of the new phase are shown in Table 7.1 alongside the results for three materials with a known hydrogen weight percent. The results show that the new phase has an elevated weight percent when compared to known oxide compounds and significantly less hydrogen content than the starting $K_2Sn(OH)_6$ precursor. The average hydrogen weight percent for the sample is 0.86 wt%, which is higher than the expected value if the composition was equivalent to the $3K_2SnO_2{\cdot}2H_2O$ phase that was predicted.

FTIR spectroscopy was performed to investigate the potential functional groups present in the new structure. $K_2Sn(OH)_6$ shows a large broad peak at 3400 cm^{-1} which characterizes the O-H vibrations in the material. The new phase, on the other hand, does not have a peak in this position and instead has a broad peak at 3210 cm^{-1}. While shifted, this peak is still in the range to describe O-H vibrations. The absence of characteristic H_2O peaks at 3600 and 1650 cm^{-1} point towards the new phase being a hydroxide rather than a hydrated compound. FTIR spectra of both phases are shown in Figure 7.2.

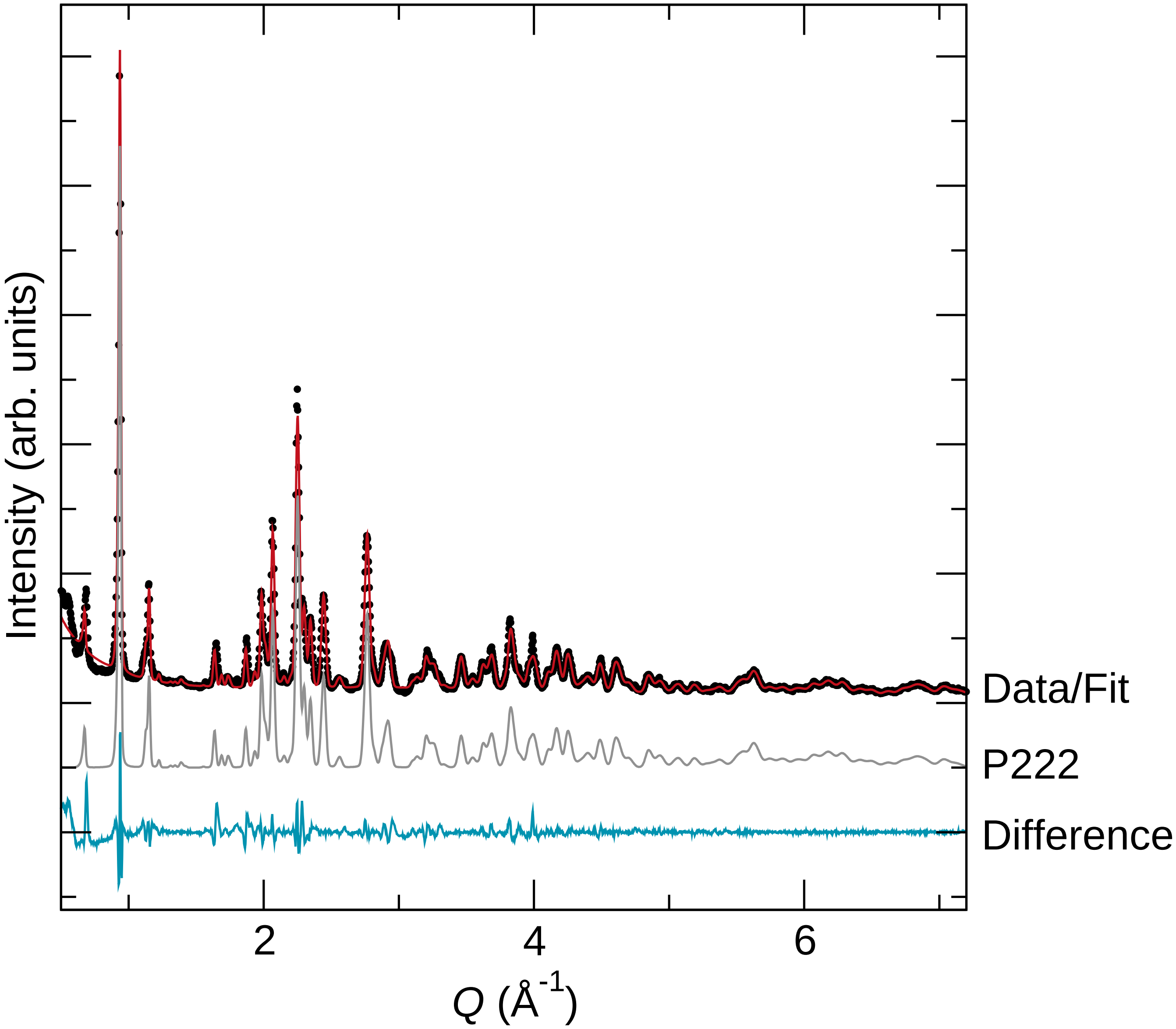

Figure 7.1: Le Bail fit to X-ray diffraction data for new phase. X-ray diffraction data was indexed to the P222 space group with a unit cell of a=13.518(2) Å, b=6.1699(7) Å, and c=9.3973(12) Å

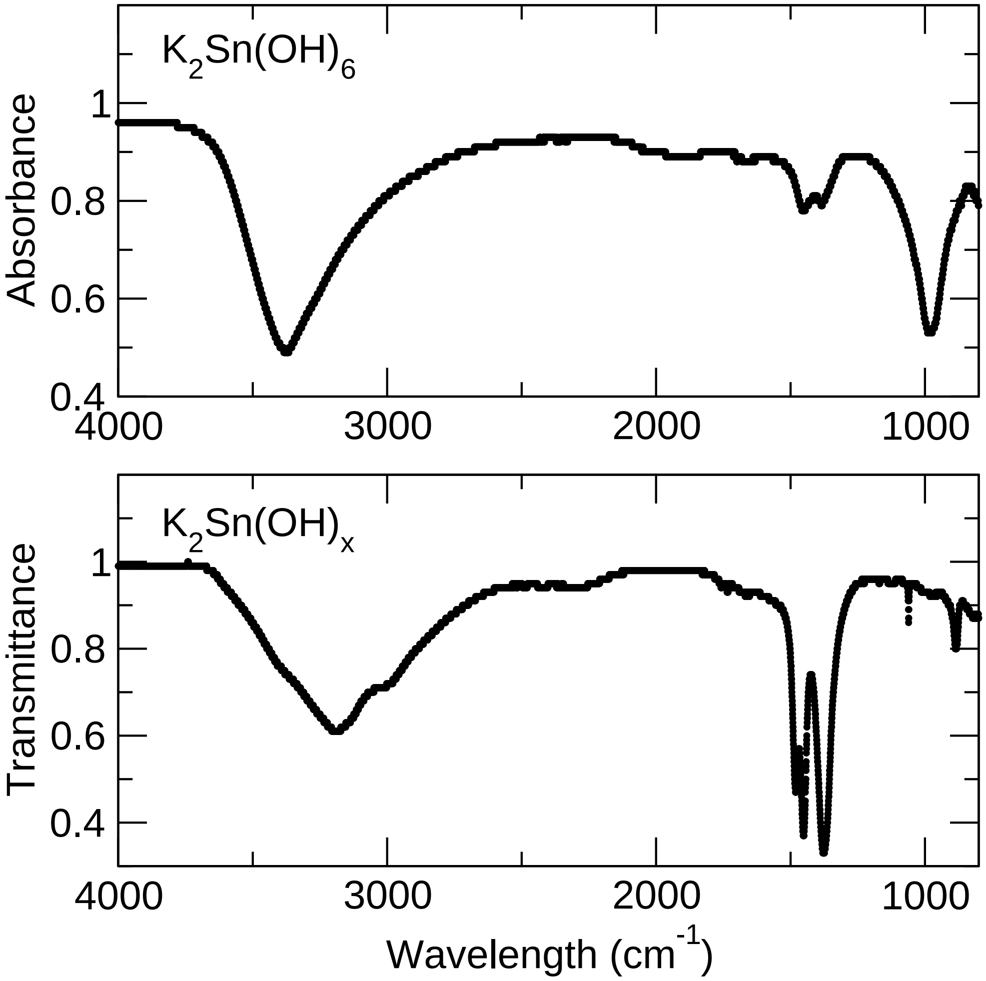

Figure 7.2: FTIR spectra of $K_2Sn(OH)_6$ (top) and of new decomposition phase, $K_2Sn(OH)_x$. (bottom)

7.4 Conclusion

During the decomposition of $K_2Sn(OH)_6$ in nitrogen, a new compound $K_2Sn(OH)_x$ was formed. This new compound is an intermediate compound between $K_2Sn(OH)_6$ and K_2SnO_3. This limits the K:Sn ratio to 2:1. The cell has been indexed to the P222 space group with a unit cell of a=13.518(2) Å, b=6.1699(7) Å, and c=9.3973(12) Å. While the structure has not been solved, complementary techniques show that the compound is a hydroxide with over half the hydrogen content when compared to the starting $K_2Sn(OH)_6$ phase.

CHAPTER 8

SUMMARY AND FUTURE DIRECTIONS

This thesis presented a systematic approach to materials discovery by combining in situ reduction and X-ray diffraction. While this approach had been utilized previously, this study focuses on the development of an in situ flow cell for rapid phase exploration can be performed without the need of a synchrotron source.

This study highlights the power of in situ reduction as a laboratory technique. While laboratory systems suffer from lower signal-to-noise, longer detection times, and lower X-ray flux than their synchrotron counterparts, the ability to perform measurements at any time can rapidly speed up a search for new compounds, The conditions tested can then be replicated at a synchrotron if higher resolution data is needed.

The in situ cell described here worked well for characterizing the systems in this study, however, small changes to the system could reduce potential variability and provide more insight into the reactions that are occurring. Adding a gas flow controller would provide a more reliable characterization of the flow rate being used throughout the reaction. Also adding a gas analyzer could provide more insight into the chemical reactions occurring within the flow cell.

In this study, the K-Sn-O system was carefully selected for phase exploration because of its potential to create *p*-type TCOs based on previous studies, it is understudied, and it has a dense energy landscape that could potentially yield new, hidden compounds. With a combination of in situ and ex situ studies, three new compounds were discovered and characterized in this system.

While only the K-Sn-O system was investigated for new compounds in this thesis, it is important to also investigate the other *A*-Sn-O systems, where *A* is an alkali element. These systems also exhibit the same characteristics that make the K-Sn-O system a good system for materials discovery. By using in situ reduction in these systems a thorough search of phase space can be performed without using the highly reactive and hygroscopic binary alkali precursors.

In situ reduction was also used to provide insight into quantifying the extent of non-stoichiometry in FeS_2. By carefully designing experiments and utilizing internal standards, a quantitative upper limit on the sulfur vacancies in pyrite FeS_2 was calculated to be 0.02% as compared to the previously published 12.5%.[59, 81]

REFERENCES

[1] Hosono, H. *Thin Solid Films* **2007,** *515,* 6000-6014.

[2] Walsh, A.; Watson, G. W. *Phys. Rev. B* **2004,** *70,* 1–7.

[3] Walsh, A.; Watson, G. W. *J. Solid State Chem.* **2005,** *178,* 1422–1428.

[4] Kawazoe, H.; Yasukawa, M.; Kurita, M.; Yanagi, H.; Hosono, H. *Nature* **1997,** *389,* 939-942.

[5] Hu, J. P.; Payne, D. J.; Egdell, R. G.; Glans, P.-A.; Learmonth, T.; Smith, K. E.; Guo, J.; Harrison, N. M. *Phys. Rev. B* **2008,** *77,* 155115.

[6] Walsh, A.; Payne, D. J.; Egdell, R. G.; Watson, G. W. *Chem. Soc. Rev.* **2011,** *40,* 4455-4463.

[7] Walsh, A.; Watson, G. W. *Phys. Rev. B* **2004,** *70,* 235114.

[8] Varley, J. B.; Schleife, A.; Janotti, A.; Van de Walle, C. G. *Appl. Phys. Lett.* **2013,** *103,*.

[9] Tournoux, M. *Ann. Chim. Fr.* **1964,** *9,* 579–600.

[10] Jansen, M.; Schon, J. C. *Angew. Chem. Int. Ed.* **2006,** *45,* 3406-3412.

[11] Bhutani, A.; Schiller, J. A.; Zuo, J. L.; Eckstein, J. N.; Greene, L. H.; Chaudhuri, S.; Shoemaker, D. P. *Chem. Mater.* **2017,** *29,* 5841-5849.

[12] Hayward, M. A.; Rosseinsky, M. J. *Chem. Mater.* **2000,** *12,* 2182–2195.

[13] Hadermann, J.; Abakumov, A. M.; Adkin, J. J.; Hayward, M. A. *Chem. Mater.* **2000,** *12,* 2182–2195.

[14] Stacy, A. M.; Badding, J. V.; Geselbracht, M. J.; Ham, W. K.; Holland, G. F.; Hoskins, R. L.; Keller, S. W.; Millikan, C. F.; Zur Loye, H. C. *J. Am. Chem. Soc.* **1987,** *109,* 2528–2530.

[15] Motohashi, T.; Takahashi, T.; Kimura, M.; Masubuchi, Y.; Kikkawa, S.; Kubota, Y.; Kobayashi, Y.; Kageyama, H.; Takata, M.; Kitagawa, S.; Matsuda, R. *J. Phys. Chem. C* **2015,** *119,* 2356–2363.

[16] Kageyama, H.; Yoshimura, K.; Kato, M.; Kosuge, K. *J. Phys. Soc. Jpn.* **1995,** *64,* 2144–2146.

[17] Hayward, M. A. *Chem. Mater.* **2005,** *17,* 670–675.

[18] Kitada, A.; Kasahara, S.; Terashima, T.; Yoshimura, K.; Kobayashi, Y.; Kageyama, H. *Appl. Phys. Express* **2011,** *4,* 18–21.

[19] Goldstein, J. I.; Newbury, D. E.; Michael, J. R.; Ritchie, N. W.; Scott, J. H. J.; Joy, D. C. *Scanning Electron Microscopy and X-ray Microanalysis;* Springer: 4 ed.; 2017.

[20] Hemming, P. E. "C,H,N Microanalysis: A comparative review of the effects of instrument design on analytical performance", accessed Oct 19 2018.

[21] Stuart, B. *Infared Spectroscopy;* Wiley: New York, 2015.

[22] van Laarhoven, P. J.; Aarts, E. H. *Simulated Annealing: Theory and Applications;* Springer: 1987.

[23] Henderson, D.; Jacobson, S.; Johnson, A. The Theory and Practice of Simulated Annealing. In , Vol. 57; Glover, F.; Kochenberger, G., Eds.; Springer: Boston, 2003; Chapter Handbook of Metaheuristics. International Series in Operations Research & Management Science.

[24] Rietveld, H. M. *J. App. Cryst.* **1969,** *2,* 65-71.

[25] Toby, B. H. *Powder Diffr.* **2006,** *21,* 6770.

[26] David, W. I. F. *J. Res. Natl. Inst.Stand. Technol.* **2004,** *109,* 107-123.

[27] Hartnagel, H., Ed.; *Semiconducting Transparent Thin Films;* Institute of Physics: Bristol, 1995.

[28] Schleife, A.; Varley, J. B.; Fuchs, F.; Rödl, C.; Bechstedt, F.; Rinke, P.; Janotti, A.; Van de Walle, C. G. *Phys. Rev. B* **2011,** *83,* 035116.

[29] Machill, S.; Shodai, T.; Sakurai, Y.; Yamaki, J.-I. *J. Power Sources* **1998,** *73,* 216–223.

[30] Sharma, N.; Plvert, J.; Subba Rao, G. V.; Chowdari, B. V. R.; White, T. J. *Chem. Mater.* **2005,** *17,* 4700–4710.

[31] Enoki, H.; Nakayama, T.; Echigoya, J. *Phys. Stat. Sol. (a)* **1992,** *129,* 181–191.

[32] Minami, T.; Sonohara, H.; Takata, S.; Sato, H. *Jpn. J. Appl. Phys.* **1994,** *33,* L1693.

[33] Belliard, F.; Connor, P. A.; Irvine, J. T. S. *Solid State Ionics* **2000,** *135,* 163–167.

[34] Raulot, J.-M.; Baldinozzi, G.; Seshadri, R.; Cortona, P. *Solid State Sci.* **2002,** *4,* 467–474.

[35] Hautier, G.; Miglio, A.; Ceder, G.; Rignanese, G.-M.; Gonze, X. *Nat. Commun.* **2013,** *4,* 2292.

[36] Iwasaki, M.; Takizawa, H.; Uheda, K.; Endo, T. *J. Mater. Chem.* **2002,** *12,* 1068–1070.

[37] Gatehouse, B. M.; Lloyd, D. J. *J. Solid State Chem.* **1970,** *2,* 410–415.

[38] Marchand, R.; Piffard, Y.; Tournoux, M. *Acta Cryst. B* **1975,** *31,* 511–514.

[39] Braun, R. M.; Hoppe, R. *Z. Naturforsch. B* **1982,** *37,* 688–694.

[40] Braun, R. M.; Hoppe, R. *Angew. Chem. Int. Ed. Engl.* **1978,** *17,* 449–450.

[41] Braun, R. M.; Hoppe, R. *Z. anorg. allg. Chem.* **1981,** *478,* 7–12.

[42] Röhr, C. *Z. anorg. allg. Chem.* **1995,** *621,* 757–760.

[43] Mesbah, A.; Oh, G. N.; Bellott, B. J.; Ibers, J. A. *Solid State Sci.* **2013,** *18,* 110–113.

[44] Favre-Nicolin, V.; Černý, R. *J. Appl. Cryst.* **2002,** *35,* 734–743.

[45] Larson, A.; Von Dreele, R. *Los Alamos National Laboratory Report* **2000,** *86,* 748.

[46] Momma, K.; Izumi, F. *J. Appl. Cryst.* **2011,** *44,* 1272–1276.

[47] McAuliffe, R. D.; Miller, C. A.; Zhang, X.; Hulbert, B. S.; Huq, A.; dela Cruz, C.; Schleife, A.; Shoemaker, D. P. *Inorg. Chem.* **2017,** *56,* 2914-2918.

[48] Uheda, K.; Horiuchi, A.; Takizawa, H.; Endo, T. *J. Porous Mater.* **1999,** *6,* 161–166.

[49] Jarzebski, Z. M.; Morton, J. P. *J. Electrochem. Soc.* **1976,** *123,* 333C–346C.

[50] Jiang, Z.; Ramanathan, A.; Shoemaker, D. P. *J. Mater. Chem. C* **2017,** *5,* 5709–5717.

[51] Nørby, P.; Johnsen, S.; Iversen, B. B. *ACS Nano* **2014,** *8,* 4295–4303.

[52] Walton, R. I.; O'Hare, D. *Chem. Comm.* **2000,** 2283–2291.

[53] Bremholm, M.; Becker-Christensen, J.; Iversen, B. B. *Adv. Mater.* **2009,** *21,* 3572–3575.

[54] Jensen, K. M.; Christensen, M.; Juhas, P.; Tyrsted, C.; Bøjesen, E. D.; Lock, N.; Billinge, S. J.; Iversen, B. B. *J. Am. Chem. Soc.* **2012,** *134,* 6785–6792.

[55] Rampelberg, G.; De Schutter, B.; Devulder, W.; Martens, K.; Radu, I.; Detavernier, C. *J. Mater. Chem. C* **2015,** *3,* 11357–11365.

[56] Readman, J. E.; Olafsen, A.; Smith, J. B.; Blom, R. *Energy Fuels* **2006,** *20,* 1382-1387.

[57] Norby, P.; Schwarz, U. Powder Diffraction: Theory and Practice. In ; Royal Society of Chemistry: 2008; Chapter Powder Diffraction under Non-ambient Conditions.

[58] Chupas, P. J.; Chapman, K. W.; Kurtz, C.; Hanson, J. C.; Lee, P. L.; Grey, C. P. *J. Appl. Cryst.* **2008,** *41,* 822–824.

[59] McAuliffe, Rebecca D., S. D. P. *Acta Cryst. B* **2018,** *74,* 436–444.

[60] Ennaoui, A.; Tributsch, H. *Solar Cells* **1984,** *13,* 197–200.

[61] Ennaoui, A.; Fiechter, S.; Jaegermann, W.; Tributsch, H. *J. Electrochem. Soc.* **1986,** *133,* 97–106.

[62] Ennaoui, A.; Fiechter, S.; Goslowsky, H.; Tributsch, H. *J. Electrochem. Soc.* **1985,** *132,* 1579–1582.

[63] Jaegermann, W.; Tributsch, H. *J. Appl. Electrochem.* **1983,** *13,* 743–750.

[64] van der Heide, H.; Hemmel, R.; van Bruggen, C. F.; Haas, C. *J. Solid State Chem.* **1980,** *33,* 17–25.

[65] Schlegel, A.; Wachter, P. *J. Phys. C: Solid State Phys.* **1976,** *9,* 3363–3369.

[66] Wadia, C.; Alivisatos, A. P.; Kammen, D. M. *Environ. Sci. Technol.* **2009,** *43,* 2072–2077.

[67] Kim, J.; Kim, G. Y.; Moon, H.; Yoon, S.; Seo, I. W.; Lee, Y.; Moon, D. G.; Ahn, S.; Jo, W. *RSC Adv.* **2016,** *6,* 81394–81399.

[68] Pascual, A.; Yoda, S.; Barawi, M.; Clamagirand, J. M.; Ares, J. R.; Ferrer, I. J.; Sánchez, C. *J. Phys. Chem. C* **2014,** *118,* 26440–26446.

[69] Zhang, X.; Scott, T.; Socha, T.; Nielsen, D.; Manno, M.; Johnson, M.; Yan, Y.; Losovyj, Y.; Dowben, P.; Aydil, E. S.; Leighton, C. *ACS Appl. Mater. Interfaces* **2015,** *7,* 14130–14139.

[70] Zhang, X.; Manno, M.; Baruth, A.; Johnson, M.; Aydil, E. S.; Leighton, C. *ACS Nano* **2013,** *7,* 2781–2789.

[71] Alonso-Vante, N.; Chatzitheodorou, G.; Fiechter, S.; Mgoduka, N.; Poulios, I.; Tributsch, H. *Sol. Energy Mat.* **1988,** *18,* 9–21.

[72] Yu, L.; Lany, S.; Kykyneshi, R.; Jieratum, V.; Ravichandran, R.; Pelatt, B.; Altschul, E.; Platt, H. A. S.; Wager, J. F.; Keszler, D. A.; Zunger, A. *Adv. Energy Mater.* **2011,** *1,* 748–753.

[73] Murphy, R.; Strongin, D. R. *Surf. Sci. Rep.* **2009,** *64,* 1–45.

[74] Rosso, K. M.; Becker, U.; Hochella, M. F. *Am. Mineral.* **1999,** *84,* 1535–1548.

[75] Herbert, F.; Krishnamoorthy, A.; Van Vliet, K.; Yildiz, B. *Surf. Sci.* **2013,** *618,* 53–61.

[76] Krishnamoorthy, A.; Herbert, F. W.; Yip, S.; Van Vliet, K. J.; Yildiz, B. *J. Phys.: Condens. Matter* **2013,** *25,* 045004-045014.

[77] Zhang, Y. N.; Hu, J.; Law, M.; Wu, R. Q. *Phys. Rev. B* **2012,** *85,* 085314.

[78] Hu, J.; Zhang, Y.; Law, M.; Wu, R. *Phys. Rev. B* **2012,** *85,* 1–10.

[79] Sun, R.; Chan, M. K. Y.; Kang, S.; Ceder, G. *Phys. Rev. B* **2011,** *84,* 035212.

[80] Fiechter, S. *Sol. Energy Mat. Sol. Cells* **2004,** *83,* 459–477.

[81] Birkholz, M.; Fiechter, S.; Hartmann, A.; Tributsch, H. *Phys. Rev. B* **1991,** *43,* 11926–11936.

[82] Ennaoui, A.; Fiechter, S.; Pettenkofer, C.; Alonso-Vante, N.; Buker, K.; Bronold, M.; Hopfner, C.; Tributsch, H. *Sol. Energy Mat. Sol. Cells* **1993,** *29,* 289–370.

[83] Brostigen, G.; Kjekshus, A. *Acta Chem. Scand.* **1969,** *23,* 2186–2188.

[84] Brostigen, G.; Kjekshus, A. *Acta Chem. Scand.* **1970,** *24,* 2993–3012.

[85] Burdett, J. K. *J. Solid State Chem.* **1982,** *45,* 399–410.

[86] Bither, T.; Prewitt, C.; Gillson, J.; Bierstedt, P.; Flippen, R.; Young, H. *Solid State Commun.* **1966,** *4,* 533–535.

[87] Krill, G.; Lapierre, M. F.; Robert, C.; Gautier, F.; Czjzek, G.; Fink, J.; Schmidt, H. *J. Phys. C: Solid State Phys.* **1976,** *9,* 761–782.

[88] Bouchard, R. J. *J. Cryst. Growth* **1968,** *2,* 40–44.

[89] Fiechter, S.; Birkholz, M.; Hartmann, A.; Dulski, P.; Giersig, M.; Tributsch, H.; Tilley, R. *J. Mater. Res.* **1992,** *7,* 1829–1838.

[90] Chatzitheodorou, G.; Fiechter, S.; Konenkamd, R.; Kunst, M.; Jaegermann, W.; Tributsch, H. *Mat. Res. Bull* **1986,** *21,* 1481–1487.

[91] Reijnen, L.; Meester, B.; Goossens, A.; Schoonman, J. *J. Electrochem. Soc.* **2000,** *147,* 1803–1806.

[92] de las Heras, C.; Martín De Vidales, J. L.; Ferrer, I. J.; Sánchez, C. *J. Mater. Res.* **1996,** *11,* 211–220.

[93] Wan, D.; Wang, Y.; Wang, B.; Ma, C.; Sun, H.; Wei, L. *J. Cryst. Growth* **2003,** *253,* 230–238.

[94] Ferrer, I. J.; Sánchez, C. *J. Appl. Phys.* **1991,** *70,* 2641–2647.

[95] Meng, L.; Liu, Y. H.; Tian, L. *J. Cryst. Growth* **2003,** *253,* 530–538.

[96] Meng, L.; Liu, M. S. *Mater. Sci. Eng., B* **1999,** *60,* 168–172.

[97] Hamdadou, N.; Khelil, A.; Bernède, J. C. *Mater. Chem. Phys.* **2003,** *78,* 591–601.

[98] Pascual, A.; Diaz-Chao, P.; Ferrer, I. J.; Sanchez, C.; Ares, J. R. *Sol. Energy Mat. Sol. Cells* **2005,** *87,* 575–582.

[99] Soukup, R. J.; Prabukanthan, P.; Ianno, N. J.; Sarkar, A.; Kamler, C. A.; Sekora, D. G. *J. Vac. Sci. Technol. A* **2011,** *29,* 011001.

[100] Wu, R.; Zheng, Y. F.; Zhang, X. G.; Sun, Y. F.; Xu, J. B.; Jian, J. K. *J. Cryst. Growth* **2004,** *266,* 523–527.

[101] Xuefeng, Q.; Yi, X.; Yitai, Q. *Mater. Lett.* **2001,** *48,* 109–111.

[102] Kar, S.; Chaudhuri, S. *Chemical Physics Letters* **2004,** *398,* 22–26.

[103] Wang, D.-W.; Wang, Q.-H.; Wang, T.-M. *CrystEngComm* **2010,** *12,* 755–761.

[104] Wilke, K.-T.; Schultze, D.; Töpfer, K. *J. Cryst. Growth* **1967,** *1,* 41–44.

[105] Nakamura, S.; Yamamoto, A. *Sol. Energy Mat. Sol. Cells* **2001,** *65,* 79–85.

[106] Kullerud, G.; Yoder, S. *Econ. Geol.* **1959,** *54,* 533–572.

[107] Momma, K.; Izumi, F. *J. Appl. Cryst.* **2008,** *41,* 653–658.

[108] Benard, J.; Jeannin, Y. Investigations of Nonstoichiometric Sulfides. In *Nonstoichiometric Compounds*, Vol. 39; Ward, R., Ed.; Washington D.C., 1963.

[109] Vegard, L. *Z. Phys* **1921,** *5,* 17-26.

[110] Lussier, J. A.; Szkop, K. M.; Sharma, A. Z.; Wiebe, C. R.; Bieringer, M. *Inorg. Chem.* **2016,** *55,* 2381–2389.

[111] Yuan, B.; Luan, W.; Tub, S.; Wua, J. *New J. Chem.* **2015,** *39,* 3571–3577.

[112] Sánchez, C.; Flores, E.; Barawi, M.; Clamagirand, J. M.; Ares, J. R.; Ferrer, I. J. *Solid State Commun.* **2016,** *230,* 20–24.

[113] Barnard, A. S.; Russo, S. P. *J. Phys. Chem. C* **2007,** *111,* 11742–11746.

[114] Höpfner, C.; Ellmer, K.; Ennaoui, A.; Pettenkofer, C.; Fiechter, S.; Tributsch, H. *J. Cryst. Growth* **1995,** 325–334.

[115] Berry, N.; Cheng, M.; Perkins, C. L.; Limpinsel, M.; Hemminger, J. C.; Law, M. *Adv. Energy Mater.* **2012,** *2,* 1124–1135.

[116] Ellmer, K.; Höpfner, C. *Philos. Mag. A* **1997,** *75,* 1129–1151.

[117] Luck, J.; Hartmann, A.; Fiechter, S. *Fresenius. J. Anal. Chem.* **1989,** *334,* 441–446.

[118] Siebert, D.; Dahlem, J.; Fiechter, S.; Hartmann, A. *Z. Naturforschung* **1989,** *44,* 59–66.

[119] Panissod, P.; Krill, G.; Lahrichi, M.; Lapierre, M. *Phys. Lett.* **1976,** *59,* 221–222.

[120] Guo, Z.; Sun, F.; Han, B.; Lin, K.; Zhou, L.; Yuan, W. *Phys. Chem. Chem. Phys.* **2017,** *19,* 9000–9006.

[121] Cabán-Acevedo, M.; Faber, M. S.; Tan, Y.; Hamers, R. J.; Jin, S. *Nano Letters* **2012,** *12,* 1977–1982.

[122] Nemudry, A.; Rudolf, P.; Schöllhorn, R. *Chem. Mater.* **1996,** *8,* 2232–2238.

[123] Andersson, K.; Nyberg, M.; Ogasawara, H.; Nordlund, D.; Kendelewicz, T.; Doyle, C. S.; Brown, G. E.; Pettersson, L. G. M.; Nilsson, A. *Phys. Rev. B* **2004,** *70,* 1–5.

[124] Vanheusden, K.; Seager, C. H.; Warren, W. L.; Tallant, D. R.; Voigt, J. A. *Applied Physics Letters* **1996,** *68,* 403–405.

[125] Murken, V. G.; Tromel, M. *Z. Anorg. Allg. Chem.* **1973,** *397,* 117-126.

[126] Toby, B. H.; Von Dreele, R. B. *J. Appl. Crystallogr.* **2013,** *46,* 544-549.

[127] Huang, Y.; Yu, Q.; Wang, J.; Li, X.; Yan, Y.; Gao, S.; Shi, F.; Wang, D.; Yu, C. *Electron. Mater. Lett.* **2015,** *11,* 1059-1065.

[128] Kim, W.-S.; Hwa, Y.; Kim, H.-C.; Choi, J.-H.; Sohn, H.-J.; Hong, S.-H. *Nano Res.* **2014,** *7,* 1128-1136.

[129] Wen Lou, X.; Wang, Y.; Yuan, C.; Lee, J. Y.; Archer, L. A. *Adv. Mater.* **2006,** *18,* 2325–2329.

[130] Jacobs, H.; Stahl, R. *Z. Anorg. Allg. Chem.* **2000,** *626,* 1863-1866.